This is the peer-reviewed, final accepted version for American Mineralogist, published by the Mineralogical Society of America.
The published version is subject to change. Cite as Authors (Year) Title. American Mineralogist, in press.
DOI: https://doi.org/10.2138/am-2022-8691. http://www.minsocam.org/

Geochemical variation in biotite from the Devonian South Mountain Batholith, Nova Scotia: Constraints on emplacement pressure, temperature, magma redox state and the development of a magmatic vapor phase (MVP)

REVISION 1

Word count: 9970

James M. Brenan[1], Bryan J. Maciag[1] and Jacob J. Hanley[2]

1) Department of Earth and Environmental Sciences, Dalhousie University, Halifax, Nova Scotia

2) Department of Geology, Saint Mary's University, Halifax, Nova Scotia

Abstract

Here we report the composition of biotite from the peraluminous Devonian South Mountain Batholith (SMB) of southwestern Nova Scotia (Canada), the largest intrusive body within the Appalachian orogen. The batholith was emplaced in two phases: an early (379-375 Ma) granodiorite-monzogranite suite (Stage 1), and a later (375-372 Ma) more evolved monzogranite-leucogranite suite (Stage 2). Biotite analyses (major and minor elements) were obtained on 55 unmineralized samples representing 11 plutons. Regardless of the stage of pluton emplacement, biotite is commonly interstitial to alkali feldspar, quartz and plagioclase, indicating similar timing of biotite saturation. This suggests that biotite chemistry records conditions at similar extents of magma evolution for the chosen suite of samples. Biotite compositions are Fe-rich, with Fe/(Fe+Mg) ranging from 0.6 to 0.98, and Al-rich, with ^{IV}Al ranging from 2.2 to 2.9 atoms per formula unit (apfu; 22 oxygen basis), the latter reflecting the coexistence of other Al-rich phases, such as muscovite, garnet, aluminosilicates and cordierite. Biotite anion sites are dominated by OH (>3 apfu), followed by F (~0.3 apfu) and Cl ($\leq$ 0.02 apfu), with a general trend of decreasing OH, increasing F and a marked decrease in Cl, with increasing differentiation.

Pressure (P) is estimated from the Al content of biotite to be between 280-430 MPa, consistent with a range of 240 to <470 MPa derived from phase equilibria and fluid inclusion microthermometry combined with mineral thermobarometry. Temperature (T) calculated from the Ti content of biotite ranges from 603-722°C. Comparison of P-T estimates with water-saturated granite phase relations suggest minimum water contents of 6-7 wt% for the SMB magmas. The redox state of the SMB was estimated by comparing biotite Fe#-Ti relations with compositions calculated using the MELTS thermodynamic model, as experiments have shown that biotite Fe# increases with decreasing fO_2 at a given extent of crystallization. Results of MELTS modelling for the most primitive magmas of the SMB sample suite indicate that the observed biotite Fe#-Ti variation is consistent with crystallization at FMQ to FMQ-1, with more oxidizing conditions suggested for the most strongly differentiated samples.

To constrain the origin of the biotite anion site variation, a quantitative model using biotite-melt exchange coefficients (K_D) derived from existing experimental data was used to track the change in

biotite OH-F-Cl abundances as a function of crystallization, with or without an extant magmatic vapor phase (MVP). The model reproduces the relative OH, F and Cl abundances in biotite, and suggests that SMB crystallization occurred in the presence of a MVP. The relatively reduced redox state of the SMB, similar to other peraluminous granitoid occurrences worldwide, aligns with other measures of fO_2 for the SMB, including the occurrence of primary ilmenite. The observed correspondence between the estimated fO_2 and that imposed by graphite-gas equilibrium suggests a role for reduced carbon in the generation and evolution of the SMB. This is consistent with evidence for SMB interaction with graphite-bearing felsic granulites of the underthrust Avalon terrane, and assimilation of carbonaceous and sulfidic metasediments during pluton ascent and emplacement.

Reducing conditions and development of a MVP have implications for granophile element concentration processes in the SMB magmatic system. Low fO_2 during crystallization affects the mineral/melt partitioning and solubility of the redox-sensitive elements Sn, W, U and Mo, serving to suppress early SnO_2 precipitation, and cause both an increase in W/Mo and an overall buildup of all four elements in evolving SMB liquids. Available experimental data indicate that reducing conditions also shifts $D^{MVP/melt}$ to favor partitioning into the melt phase. Therefore, early vapor exsolution under reducing conditions also lessens the extraction efficiency of these redox-sensitive elements to the MVP, further underscoring the role of extensive crystallization as an important metal enrichment process.

Key words: biotite, halogens, peraluminous granite, South Mountain Batholith, oxygen fugacity

1.0 Introduction: Biotite as an indicator of magmatic conditions

The mineral biotite, represented by the annite (Fe^{2+})-phlogopite (Mg^{2+}) substitution formula $K(Mg_{0.6\text{-}1.8}Fe_{2.4\text{-}1.2})(Si_3Al)O_{10}(OH,F,Cl)$, is a trioctahedral mica, with common replacement of the octahedrally-coordinated Mg and Fe^{2+}, with Al^{3+} (eastonite-siderophyllite substitution), Fe^{3+}, and a number of similarly-sized cations, such as Li, Ti, V, Cr, Mn, Co, Ni, Cu, Sn and Zn (Groves, 1972; Bailey, 1984; Tischendorf et al., 2001). This mineral is ubiquitous in granitoid rocks, and biotite compositional variation can yield diverse information about the prevailing conditions during magma evolution. If coexisting with either magnetite or ilmenite (+ K-feldspar), biotite Fe-Mg-Fe^{3+} or Ti contents yield quantitative constraints on magma oxygen fugacity (fO_2), temperature (T) and water fugacity (fH_2O; Wones and Eugster, 1965; Patino-Douce, 1993). The Ti content of biotite also provides biotite-formation temperatures (Patino-Douce, 1993; Henry and Guidotti, 2002; Henry et al., 2005; Chambers and Kohn, 2012) in Ti "saturated" rocks, containing ilmenite or rutile, whereas pressure can be estimated from biotite Al concentrations (Uchida et al., 2007). For systems in which a melt composition can be estimated, biotite-melt Fe-Mg exchange is also a function of magma fO_2 (Bucholz et al., 2018), whereas biotite-melt partitioning of Ti can also be used to estimate the biotite-forming temperature (Righter and Carmichael, 1996). Substitution of OH, F and Cl into the biotite anion site provides information on halogen concentration changes in the melt phase (Icenhower and London, 1997; London,

1997; Zhang et al., 2022), and also the relative fugacity of HF (fHF) to fH_2O (Munoz and Ludington, 1974). Fluorine-OH exchange between biotite and apatite is also a useful thermometer (Stormer and Carmichael, 1971; Ludington, 1978; Zhu and Sverjensky, 1991; Sallet, 2000).

The above constraints on magma evolution may also provide important information on the development of associated metallogeny. For example, magma fO_2 dictates the speciation of redox-sensitive elements, such as Fe and S, which impacts the relative propensity for metal-concentrating sulfide and oxide minerals vs. metal-poor sulfates and oxides to form, and the specific composition of the saturated mineral phase (Sisson and Grove, 1993; Toplis and Carroll, 1995; Jugo et al., 2005; Carroll and Rutherford, 1988). The solubility, and fluid-melt/mineral-melt partitioning of some granophile ore metals, such as Sn, W, Mo and U, have also been shown to be sensitive to fO_2 (Candela and Bouton, 1990; Taylor and Wall, 1993; Linnen et al., 1995; 1996; Pieffert et al., 1996; Farges et al., 2006; Bali et al., 2012; Fonseca et al., 2014). A magmatic volatile phase (MVP) can serve as an important medium for ore metal sequestration and transport, and the timing of MVP formation relative to the extent of crystallization is a critical factor in concentrating granophile ore metals (Candela and Holland, 1986; Cline and Bodnar, 1991; Audetat and Pettke, 2003; Audetat et al., 2008; Zajacz et al., 2008; Webster et al., 2018; Dolejš and Zajacz, 2018; Pirajno, 2018; Audetat, 2019). Owing to differences in the fluid-melt partitioning of F and Cl (summarised in Baker and Alletti, 2012), the development of a MVP may significantly change the system mass balance of these elements, which would be recorded in the coexisting biotite composition (e.g., Zhang et al., 2012; Berni et al ., 2017; Li et al., 2020). As well, variations in biotite halogen chemistry may also reflect the relative Cl-F-H_2O concentrations in the evolving MVP, which is important to granophile ore metal complexing (Manning and Henderson, 1984; Keppler and Wyllie, 1991; Taylor and Wall, 1993;; Bai and Koster Van Groos, 1999; Audetat and Pettke, 2003; Williams-Jones and Heinrich, 2005; Audetat et al., 2008; Zajacz et al., 2008; Webster et al., 2018; Dolejš and Zajacz, 2018; Pirajno, 2018; Audetat, 2019).

In this context, we report on the biotite chemistry of the late Devonian, peraluminous South Mountain Batholith (SMB) of mainland Nova Scotia (Figure 1). Outcropping over 7300 km^2, it is the largest granitoid body in the Appalachian orogen. Biotite is an ubiquitous phase in the SMB, with consistent paragenetic relations, providing a window on magma chemistry at similar stages in the sample crystallization history. We have measured a geochemically-diverse suite of major, minor and trace elements including the alkali metals (Li, Rb, Cs), alkaline earth metals (Sr, Ba), transition metals (Sc to Mo), rare-earth elements (REE), high field strength elements (Ti, Nb, Ta, Hf, Zr, W), as well as the

semi-metals (Ga, In, Sn, Bi, As, Pb) and halogens (Cl, F). We provide these biotite compositional data in a two-part series, with part one, presented here, documenting biotite major and minor element chemistry, with implications for intensive parameters, and the development of a MVP during SMB magmatic evolution. Results on biotite trace element compositions will be reported elsewhere.

2.0 Geological setting and overview of the South Mountain batholith

The South Mountain batholith is located in the Meguma Lithotectonic zone (Figure 1), which is the most outboard allocthonous terrane of the northern segment of the Appalachian orogenic belt in Atlantic Canada (Williams, 1979). The terrane is separated from the Neoproterozoic-Cambrian composite Avalon zone to the north by the east-trending Cobequid-Chedabucto Fault Zone (CCFZ). The Meguma Lithotectonic zone comprises both a suite of mafic to felsic intrusive rocks and a package of sedimentary rocks. At the base of the stratigraphy is the Cambrian-Ordovician Meguma Supergroup, a flysch sequence that includes a lower part dominated by fine-grained graywacke, the Goldenville Formation, and the upper Halifax Formation, comprised of pyritic slate with interbedded siltstone and argillite (Schenk 1995a; Waldron 1992). The Meguma Supergroup is overlain by mixed sedimentary and mafic-felsic volcanic rocks of the Silurian to Devonian White Rock, Kentville, New Canaan and Torbrook formations, all of which were deposited in shallow water continental settings (Schenk, 1995b). The entire succession was regionally deformed and metamorphosed during the Acadian Orogeny at 400-375 Ma (Keppie and Dallmeyer 1987; Kontak et al. 1998; Hicks et al. 1999). Deep seismic reflection profiles show that the Meguma Supergroup and associated igneous rocks overlie, at mid-crustal depths, a seismically distinct lower crustal block, termed the Sable block by Keen et al. (1991). Granulite facies xenoliths (termed Tangier lower crust) which have been transported to the surface by late Devonian mafic intrusive bodies (Tate and Clarke, 1995) reveal younger Nd model ages than Meguma Supergroup sediments, indicating a time-inverted stratigraphy, and the interpretation that the Sable block is affiliated with the adjacent Avalon Lithotectonic zone (Eberz et al., 1991).

Magmatism in the Meguma Lithotectonic zone ranges in age from Mid Devonian to Early Carboniferous (385-357 Ma; e.g., Shellnutt and Dostal, 2019) and includes relatively large (10s to 1000s of km^2) granitoid intrusive bodies as well as minor mafic intrusions that occur as dykes, plugs, and synplutonic bodies of gabbro, diorite, or lamprophyre (de Albuquerque, 1979; Tate and Clarke, 1995; Shellnutt and Dostal, 2019). The granitoid intrusions have been subdivided as “Central” (including the SMB) or “Peripheral” based on systematic differences in mineralogy, chemistry and isotopic characteristics (Tate and Clarke, 1997). The SMB has been delineated into 49 map units, assigned to at

least 11 individual plutons which constitute two intrusive stages (Figure 1). The six main rock types comprising the SMB are: 1) biotite granodiorite, 2) biotite monzogranite, 3) muscovite-biotite monzogranite, 4) coarse and 5) fine-grained leucomonzogranite and 6) leucogranite (MacDonald, 2001). Early (stage 1) biotite granodiorites to monzogranites were emplaced between ~379 to 375 Ma and later (stage 2), more chemically-evolved leucomonzogranite to leucogranite yield ages spanning ~375 to 372 Ma (autocrystic zircon U-Pb zircon; Bickerton et al., 2022). Earlier antecrystic zircon yields ages up to 15 Ma older than the SMB emplacement, which together with age data from autocrystic grains suggests a ~20 Ma window for magmatic activity related to SMB evolution (Bickerton et al., 2022). Some of the later stage 2 plutons are associated with polymetallic mineral deposits, most notably at East Kemptville (Sn–Zn–Cu–Ag; Kontak, 1990; Halter et al., 1995; 1996; 1998; Bickerton, 2021) and New Ross (Cu-Mo-Mn-Sn-U-W; Carruzzo et al., 2000; 2004).

Compositionally, the SMB is peraluminous, with molar $Al_2O_3/CaO+Na_2O+K_2O$ (A/CNK) ranging from 1.16 to 1.23. Concentrations of SiO_2 range from ~67-74 wt% and track a remarkably continuous differentiation sequence, with decreasing TiO_2, FeO, MnO, MgO, CaO and K/Rb defining the evolution from SiO_2-poor biotite granodiorites to SiO_2-rich leucogranites. There is a similarly continuous covariance of trace incompatible (Rb, Ta, U, Li, F, Sn, W) and compatible (Ba, Sr, Zr, V, Hf, Sc, REE) elements (MacDonald, 2001). Model results indicate that the observed range of major element and trace element compositions is consistent with a combination of assimilation and fractional crystallization (AFC) processes (Clarke et al. 2004; Shellnutt and Dostal, 2012; 2015). In addition to abundant quartz and feldspars, SMB samples contain varied abundances of biotite, muscovite, aluminosilicates (sillimanite or andalusite), cordierite, garnet and tourmaline, reflecting the peraluminous nature of the SMB-forming magmas. Ilmenite is an ubiquitous accessory phase, and primary magnetite is absent (MacDonald, 2001).

3.0 Materials and Methods

3.1 Sampling

Samples were obtained from field work in 2018 and 2019 conducted by J. Brenan, J. Chavez and B. Maciag, and from the NS Department of Natural Resources and Renewables sample archive at the Nova Scotia Core Library in 2020 and 2021. A primary goal of this study was to document biotite compositions from different granitoid compositions from across the SMB to establish the baseline compositional characteristics of unmineralized samples. The Nb/Ta ratio has been suggested to

discriminate between felsic igneous rocks whose composition is largely dictated by magmatic crystallization, and those modified by interaction with a mineralizing fluid phase (Dostal and Chatterjee, 2000; Ballouard et al., 2016; 2020). We therefore used the whole-rock Nb/Ta ratio for initial screening amongst samples likely dominated by purely magmatic processes ($\geq$ 5) vs. those suspected to be modified by fluids (< 5). Geochemical data for the screening were obtained from the Nova Scotia Department of Natural Resources and Renewables database for the SMB (MacDonald, 2001) as well as our own previous work (Chavez, 2018). We identified 55 samples for analysis from six stage 1 plutons and five stage 2 plutons, with the distribution of samples across the SMB shown in Figure 1. Of the 55 samples, all but five have Nb/Ta $\geq$ 5, allowing us to establish trends in biotite chemical variation that can be attributed to magmatic processes, and also to assess the extent to which low Nb/Ta samples deviate from those trends. Table 1 provides a summary of the samples, including grid coordinates, pluton occurrence, lithology and relevant textural information (further details on biotite textures are provided in section 4.1).

3.2 Analytical methods

Analyses of biotite from SMB samples were performed on polished thin sections that ranged in thickness from ~30-100 micrometers. Typically, one thin section was made per sample, and individual sections were cut into smaller pieces to isolate biotite-rich domains, allowing for more samples to be loaded into the electron microprobe or laser ablation sample chamber. The general analytical protocol involved an initial sample survey by petrographic microscope to document biotite textural attributes. Sample maps at a magnification of 20x were then acquired by digital image acquisition of areas containing the biotite chosen for subsequent analysis. Trace element analyses by laser ablation ICP-MS (results reported separately) were always performed first, with specific analytical sites documented on the sample maps. Following trace element analysis, section fragments were then subjected to a brief polish with 0.3 micrometer alumina to remove any adhering aerosol deposits, cleaned ultrasonically, and then carbon-coated for subsequent electron microprobe analysis and scanning electron microscopy. Details of these analytical methods are provided in the On-Line Material. A full list of biotite analyses is provided in Table S1, with a summary of major and trace element whole-rock analyses, as well as analyses from the Department of Natural Resources and Renewables database and external standard reference materials, is provided in Tables S2 and S3.

4.0 Results

This is the peer-reviewed, final accepted version for American Mineralogist, published by the Mineralogical Society of America.
The published version is subject to change. Cite as Authors (Year) Title. American Mineralogist, in press.
DOI: https://doi.org/10.2138/am-2022-8691. http://www.minsocam.org/

4.1 Summary of biotite textural types from the South Mountain Batholith

Sample textures ranged from broadly equigranular to porphyritic with alkali feldspar + quartz ± plagioclase porphyrocrysts (summarized in Table 1). In both stage 1 and 2 plutons, biotite occurs as an interstitial phase, and relatively late in the paragenetic sequence in the majority of samples studied (Figures 2 and 3). Modal abundance of biotite is higher in stage 1 plutons (avg. ~9 vol%; range of 3-15 vol%) compared to stage 2 plutons (avg. ~4 vol%; range of 1-10 vol%). Most commonly, biotite is interstitial to alkali feldspar, quartz, plagioclase and primary muscovite, showing cuspate-lobate intergrowths with these minerals, indicating late biotite growth. In some samples, alkali feldspar, quartz and biotite appear to be coeval, suggesting earlier biotite formation in these cases. The latter biotite occurrence is observed in samples from both stage 1 and 2 plutons and is not unique to any specific pluton. Combined with observations from other samples where biotite is interstitial, these observations suggest a protracted crystallization history for biotite in the SMB. Primary muscovite and plagioclase are not coeval with biotite. Secondary chlorite (Figure 2A) and muscovite commonly replace biotite. Chloritization of biotite varies in intensity from negligible to pervasive (see Table 1). Secondary muscovite alteration also varies in intensity with some relict biotite grains showing sharp grain contacts with enclosing replacive muscovite (e.g., Figure 2B). Other biotite grains have epitaxitic overgrowths (Figure 2G-H), composed of an intermediate mica phase (IMP) depleted in Fe and enriched in Mg relative to the biotite, and an outer rim of muscovite. This textural sequence was interpreted by Clarke and Bogutyn (2003) to be produced by intermittent episodes in which the pressure exceeded $P_{lithostatic}$, and $a_{H2O} = 1$, causing fluctuations in the stability of biotite and muscovite relative to IMP.

Accessory mineral inclusion abundance in biotite is highly variable; in some samples, these accessory phases are rare, whereas in others, biotite contains very abundant inclusions. Included accessory phases are up to 3 times more abundant in stage 1 than in stage 2 plutons. The most common accessory phases are zircon, ilmenite, and apatite with lesser amounts of monazite and allanite (c.f. Clarke et al., 2021). These phases occur as inclusions in, rimming and surrounding biotite (Figure 2A,B, Figure 3A-C). Textural relations indicate that these phases were saturated both before and during biotite growth.

In addition to differences in accessory mineral inclusion abundance, some notable differences exist between biotite in stage 1 and stage 2 plutons. In stage 1 plutons, plagioclase in contact with biotite is strongly zoned to more albitic compositions (shifts from labradorite-andesine to oligoclase-albite, usually approaching albite end-member at the biotite grain contact; Figure 3D-G). Along these

biotite contact areas other coronitic reaction textures are common, comprised of an intergrowth of alkali feldspar, quartz, biotite and ilmenite (Figure 3D-G). The plagioclase zoning and this reaction texture were not observed in stage 2 plutons. In stage 2 plutons, plagioclase-biotite grain boundaries are stable (e.g., Figure 2A). However, in stage 2 plutons, a symplectic intergrowth of alkali feldspar, quartz and biotite was commonly observed where alkali feldspar and biotite are in contact with one another (Figure 2C, E). Additionally, the presence of epitaxial overgrowths of IMP and muscovite are more common in stage 2 plutons. The corona and symplectites observed are suggestive of subsolidus reaction textures such as those observed in metamorphosed and hydrothermally altered granitoids (cf. Rubbo and Bruno, 2003; Zhang et al., 2021) and do not imply that the minerals involved were coeval in the original magmatic rock.

4.2 Chemical variation of biotite within the South Mountain Batholith

4.2.1 Biotite major element composition and classification

In general, biotite in individual samples is relatively homogeneous with respect to major and minor elements, with average relative standard deviations of ~10% for Ti and Mn, 5% for Mg and 2% for Al and Fe. Figure 4 summarizes the SMB biotite compositions in terms of the proportion of tetrahedral aluminum (Al^{IV}, calculated on the basis of 22 oxygens) as a function of the molar Fe/(Fe + Mg) (Fe#), with a comparison to biotite in Paleozoic granitic rocks from the Meguma and other lithotectonic zones of the Canadian Appalachians and peraluminous plutons hosting intrusion-related Sn-W-(Cu-As) mineralization from Cornwall (Cornubian granites; see the caption to Figure 4 for sample references). SMB biotites are all relatively iron-rich (Fe# 0.6 to 0.98), with stage 2 samples having systematically higher Fe# compared to those from stage 1. The proportion of Al^{IV} is similar between Stage 1 and Stage 2 samples, and significantly exceeds the annite-phlogopite binary. Both of these compositional characteristics are similar to biotite from other peraluminous granites. Within the Meguma terrane, the SMB biotite overlaps with the Musquodoboit batholith central intrusion, in terms of high Al^{IV} and Fe# (MacDonald, 1981). The Port Mouton and Queensport peripheral intrusions reflect a continuum of Al^{IV} from less than to similar to the SMB, with mostly overlapping Fe# (Figure 4a; Douma, 1988; Ham, 1988). Compared to the other suites portrayed (Figure 4b), although there is a general overlap in Al^{IV}, the SMB compositions trend to more extreme levels of Fe enrichment. Whereas the differences in Fe# from stage 1 to stage 2 plutons agree with the expected change in biotite composition along a magmatic differentiation trend, the elevated Al^{IV} content reflects the high A/CNK of the SMB-forming magma (Clarke, 1981).

4.2.2. Halogen geochemistry

Figure 5a portrays a summary of calculated biotite OH, Cl and F endmember proportions on a ternary OH/10-Cl*10-F diagram. Also included for comparison (Figure 5b) is the subset of occurrences portrayed in Figure 4 for which biotite halogen abundances are reported. In general, biotite from the SMB, as well as the other locations portrayed, are OH-rich and F-poor, with compositions ranging from Cl-free to F/Cl of <0.25. Biotite from the SMB define two distinct trends; the first (hereafter, trend 1) is roughly parallel to the OH-Cl join, at constant F content and the second (hereafter trend 2) is defined by decreasing Cl (and OH) relative to F, extending towards the F apex. Although both arrays show some overlap in terms of pluton type, trend 1 comprises mostly Stage 1 pluton samples, whereas trend 2 is dominated by those from Stage 2. Such trends are remarkably similar to those observed in other peraluminous Appalachian granite suites, as well as in Cornwall granites. Suites that exhibit the trend 1 array include the unmineralized and Cu-Mo mineralised granites of the Saint George batholith (Avalon zone) and the New Brunswick Central Magmatic belt (Gander zone). Granite suites that exhibit trend 2 include Mt. McGerrigle (Humber zone), Sn-W-Mo-mineralised granites of the New Brunswick Central Magmatic belt, and Sn-(Cu-As) mineralized Cornubian granites at Land's End, Cornwall, U.K. As mentioned earlier Sn-W-Mo mineralization is also associated with Stage 2 plutons from the SMB, notably the East Kemptville Sn deposit associated with the Davis Lake pluton (Kontak, 1990; Halter et al., 1995; 1996). The apparently unique association between Sn mineralization and trend 2 may reflect a process-related link, and could be a useful guide in an exploration context. Notably, whereas some barren suites also show biotite with Trend 2 compositions, biotite from many mineralized plutons including those in the SMB and Cornwall fall along trend 2 arrays that reach far greater extremes in F enrichment, approaching end-member fluorbiotite in the latest/most evolved granitoid samples. The origins of both halogen trends are explored in section 5.2 in the context of biotite crystallization models which take into account the presence or absence of a magmatic vapor phase.

4.3 Estimation of intensive parameters

4.3.1 Biotite crystallization pressure, temperature and melt water content

The pressure of biotite crystallization is estimated from the results of Uchida et al. (2007), who developed a geobarometer using correlations between the total Al content of biotite (Al^{total}) and pressures determined by sphalerite and Al-in-hornblende barometry. The resulting relationship is:

$$P\ (MPa) = (3.03 \times Al^{total} - 6.53)*100 \qquad (1)$$

from which calculated pressures for the SMB are in the range from ~280 to 430 MPa (Table A1).

Constraint on biotite crystallization temperature is based on the Ti content and Mg/(Mg+Fe) of biotite coexisting with either ilmenite or rutile, after the method of Henry et al. (2005), using the relationship:

$$T(^{o}C) = (((\ln(Ti) + 2.3594 - 1.7283*(Mg/(Mg+Fe))^{3})/4.6482x10^{-9})^{0.333} \quad (2)$$

where Ti is atoms per formula unit, and Mg/(Mg+Fe) are in molar units. The applicable compositional range for this thermometer is for Ti between 0.04 and 0.60 apfu, and Mg/(Mg+Fe) between 0.275 and 1 (Henry et al., 2005). All of the SMB biotites are within the calibrated Ti range, but some are too Fe-rich for the calibration, and therefore excluded. Based on petrographic observations, ilmenite ± rutile is a ubiquitous phase assemblage in the samples studied, although in some cases these minerals have been shown to be xenocrystic (Clarke and Carruzzo, 2007). Temperatures obtained from this method are in the range of 603 to 722°C, and show a correlation between decreasing temperature and other measures of differentiation, such as whole-rock SiO_2 (not shown) and biotite Ti concentration (Figure 6a). As it is expected that the crystallization of ilmenite and coexisting biotite will deplete the melt in TiO_2 during cooling and crystallization (rutile crystallization would have a similar effect, although the observed abundances of rutile are significantly less than ilmenite), the observed correlation is, therefore, consistent with crystallization during cooling. In support of ilmenite as a fractionating phase throughout the SMB, we also note the strong correlation between decreasing TiO_2 with increasing SiO_2 in the SMB whole-rock data (Table A2).

Holtz et al. (1995) summarized the effect of pressure, temperature and total water content on the water-saturated solidus and liquidus of metaluminous granitic compositions to derive lower bounds on melt water contents. Assuming whole-rock compositions approximate a liquid, the P-T conditions of each sample is compared to the liquidus curves for different water contents in Figure 6b, with most samples consistent with minimum water contents of 6 to 7 wt%. As noted by Holtz et al. (1995), melts that are more peraluminous than the calibration dataset yield higher water solubilities at a given P and T, suggesting that the minimum water contents derived from Figure 6b are conservatively low estimates.

4.3.2 Biotite Fe#-Ti relations and SMB magma redox state

Oxygen fugacity is a parameter that affects element behavior during magma evolution, including melt-crystal and -fluid partitioning and mineral solubility. The presence of ilmenite and/or rutile coexisting with biotite in most of the SMB samples studied offers the potential for two independent

redox sensors (Zhao et al., 1999; Patino Douce, 1993). In the present study we estimate fO_2 based on the variation in biotite Fe#. As shown in Figure 7, the Fe# in biotite increases with decreasing Ti concentration, which was shown in the previous section to be a measure of falling temperature. Samples with Nb/Ta ratios < 5 overlap with the Fe#-Ti range shown by the other samples, although there is a tendency for the latter group to have lower Ti and higher Fe#. Previous experimental studies on peraluminous and peralkaline silicic compositions (Dall'Agnol et al., 1999; Scaillet & Evans, 1999; Costa et al., 2004; Icenhower & London, 1995; Bogaerts et al., 2006; Mutch et al., 2016; Scaillet & Macdonald, 2001, 2003; Scaillet et al., 1995) have also shown that biotite Fe# increases with decreasing temperature, consistent with the variation seen in the SMB samples. Another important result of those experimental studies is that, at a given temperature, the biotite Fe# increases with decreasing fO_2, consistent with a shift to the left of the heterogenous redox equilibrium:

$$KFe^{2+}{}_3AlSi_3O_{10}(OH)_2 + 0.75O_2 = KAlSi_3O_8 + 1.5Fe_2O_3{}^{melt} + H_2O \quad (3).$$

Bucholz et al (2018) used the MELTS thermodynamic model and applied equation 3 to successfully reproduce the shift in Fe# with fO_2 for biotite from the aforementioned experiments. We have taken a similar approach to estimating the redox state of SMB samples and used the MELTS model to monitor biotite Fe# during crystallization of select SMB compositions at fO_2 corresponding to the fayalite-magnetite-quartz (FMQ) oxygen buffer, as well as FMQ +/- 1. Details of the model are provided in the Online Material.

Comparison of the model crystallization curves with measured biotite compositions (Figure 7) suggests that most SMB biotites crystallized at fO_2 between FMQ and FMQ-1, but with some high Ti exceptions that crystallized at systematically higher *f*O2 than FMQ (e.g., Five Mile Lake pluton). Biotites from the New Ross Pluton record the largest range of compositions, corresponding to a shift in fO_2, from the most evolved samples (lowest Ti, highest Fe#) reflecting crystallization at more oxidized conditions (near FMQ) to less evolved samples (near FMQ-1). Overall, these results are consistent with the presence of ilmenite in SMB samples, rather than coexisting rhombohedral and cubic oxides, as would be expected at fO_2 at or above FMQ (Toplis and Carroll, 1995; Dall'Agnol et al., 1999). Moreover, with the exception of a brief (14°C) temperature interval of magnetite crystallization for the Halifax Pluton composition, the MELTS model crystallizes ilmenite as the only oxide phase at FMQ-1, in contrast to both oxides forming in models run at FMQ and FMQ+1.

This is the peer-reviewed, final accepted version for American Mineralogist, published by the Mineralogical Society of America.
The published version is subject to change. Cite as Authors (Year) Title. American Mineralogist, in press.
DOI: https://doi.org/10.2138/am-2022-8691. http://www.minsocam.org/

The MELTS modelling results also predicts a decrease in biotite Fe#, and Ti content with decreasing temperature. The crystallization interval required to produce the biotite Fe#-Ti relations is 780-660°C for the FMQ and FMQ-1 models, which covers the range of 722-603°C recorded by the Ti-in-biotite thermometer of Henry et al. (2005). As the most Fe-rich biotites are outside of the calibration range of the Henry et al. (2005) thermometer, but likely represent the most evolved samples, the actual biotite crystallization interval may persist to even lower temperatures. Assuming that the highest temperature for biotite crystallization produced by the MELTS model is accurate, the lower maximum temperature recorded by the SMB biotites could reflect subsolidus re-equilibration.

5. Discussion

5.1 Comparison to other constraints on emplacement pressure and magma redox state

A variety of other methods have been used to constrain the depth, and hence pressure, of the current exposure level of the SMB, which yield broadly consistent results with estimates from biotite chemistry. Jamieson et al. (2012) report on the textures and mineral assemblages developed in contact-metamorphosed low and high Al metapelites (Bluestone and Cunard formations, respectively) of the Halifax member of the Meguma supergroup in intrusive-contact with the SMB. The presence of the assemblage andalusite (± fibrolitic sillimanite) + biotite + K-feldspar ± cordierite, and evidence for incipient partial melting, constrains a pressure range from 250 to 300 MPa (at ~650°C). This result was corroborated by Hilchie and Jamieson (2014) based on thermal modelling of temperature profiles from across the aureole obtained from graphite thermometry on the same lithologies. Another pressure estimate based on constraints from SMB-related lithologies is derived from the East Kemptville leucogranite, which is associated with the stage 2 Davis Lake pluton, and hosts Sn-bearing greisens formed during magma emplacement (Halter et al., 1995; 1996). Halter and Williams-Jones (1999) constrained the pressure of greisen formation between 240 and 400 MPa based on the intersection of temperatures estimated from the topaz-muscovite thermometer and fluid inclusion isochores. As a direct estimate from the SMB mineralogy, Clarke et al. (1976) derived a pressure of less than 470 MPa based on the presence of magmatic andalusite, and the intersection of the second sillimanite isograd with the water-saturated granite minimum. Considering all constraints summarized here, an estimate for the emplacement pressure at the current level of exposure is in the range of ~240 to 470 MPa.

In terms of other redox estimates for the SMB, Bickerton et al. (2022) documented fO_2 ranging from FMQ to FMQ-5 based on the Ce-in-zircon oxygen barometer of Smythe and Brenan (2016) for a

similar suite of samples to those investigated in this study. This is in broad agreement to the results documented here, in terms of samples being relatively reduced, although FMQ-5 is close to the lower stability limit of Fe-rich biotite (Eugster and Wones, 1962). Shabani et al. (2003) estimated fO_2 from SMB samples based on biotite Fe^{3+}/Fe^{2+} (determined by Mossbauer spectroscopy) and Fe# relations, comparing to the experimental results of Wones and Eugster (1965). The fO_2 documented in that case was in the range of FMQ to ~FMQ+0.5, but the lack of magnetite in the samples studied limits these estimates to maximum values. In general, the fO_2 range for the SMB documented here is more reduced than estimates for other granites from the Canadian Appalachians described by Shabani et al. (2003), who report values more oxidized than FMQ. Not included in the Shabani et al. (2003) compilation are the Late Silurian to Late Devonian granite suites emplaced into the Avalon Zone of southwestern New Brunswick, whose fO_2 has been documented in detail by Yang and Lentz (2005). Estimates of fO_2 used the same method as Shabani et al (2003), although Fe^{3+} was determined from stoichiometry, and the approach of Ague and Brimhall (1988) was used in cases where ilmenite was present in the absence of magnetite. Results reveal that the earlier (Late Silurian-Early Devonian) granodiorite to monzodiorite series contain both relatively reduced (FMQ-1 to -2) and oxidized (~FMQ+2) members, whereas the later (Late Devonian) granitic series is uniformly relatively reduced (~FMQ-2).

5.2 Origin of the Type 1 and Type 2 F-Cl-OH compositional trends

In order to better understand the origins of the F-Cl-OH compositional trends exhibited by the SMB biotite, we attempt to quantify this behavior by exploring different crystallization scenarios using available biotite-melt-fluid partitioning data for the halogens and water. To more clearly define the trends in F-Cl-OH behavior with magma evolution, we use the Ti content of biotite to track the extent of crystallization, as this is a minor element that is expected to show approximately constant biotite-melt partitioning, and tracks with the biotite Fe/Fe+Mg (Figure 7) as well as decreasing temperature (Figure 6a). The change in biotite F-Cl-OH with Ti concentration is portrayed in Figure 8a, and although there is some scatter to the data, trends of decreasing OH and Cl, and increasing F, with decreasing Ti, are relatively well defined. Consistent with the data plotted in the OH/10-Cl*10-F ternary diagram (Figure 5), Stage 1 pluton biotite tends to have higher Cl and OH, and lower F, than the Stage 2 biotite. In terms of the expected behavior of F and Cl during crystallization, both elements are compatible in biotite (F into Mg-rich biotite, and Cl into Fe-rich biotite; Munoz and Luddington, 1974; Munoz, 1984; Volfinger et al., 1985; Zhu and Sverjensky, 1992; Icenhower and London, 1997; Mi and Pan, 2018). Apatite is the only other significant halogen-bearing phase observed in our SMB suite of samples, with apatite/melt

partition coefficients for both F and Cl $\geq$1 (Mathez and Webster, 2005; Webster et al., 2017). However, Cl and F are likely to be strongly incompatible in the predominant crystallizing phases (quartz, feldspar) based on the results of previous mineral/melt partitioning experiments involving other nominally anhydrous minerals (plagioclase, olivine, pyroxene; Dalou et al., 2012; Hauri et al., 2006). Given the low modal abundance of apatite and biotite in SMB samples, the bulk partition coefficients (defined as the sum of the products of individual mineral-melt partition coefficient and respective mass fractions in the crystallizing assemblage) for Cl and F will be less than one. Both elements will, therefore, increase in concentration during fluid-absent crystallization. In that context, although the observed increase in F is qualitatively consistent with predictions, the depletion in Cl with decreasing Ti observed in SMB biotites is inconsistent with an expected build-up in melt chlorine abundance. In contrast to uniformly incompatible behavior in the bulk crystallizing solid assemblage, F and Cl are fractioned differently by a magmatic vapor phase (MVP). As reviewed in Baker and Alletti (2012) and Dolejš and Zajacz (2018), previous experimental studies have shown that Cl partitions strongly into one or more coexisting MVP, with the composition of the exsolving MVP influenced by the melt Cl/H_2O ratio, P and T. In contrast to Cl, F shows greater compatibility for the silicate melt phase and F concentration in an exsolved MVP varies as a function of the Aluminum Saturation Index (ASI) and F concentration of the melt. Hence, generally, the separation of a MVP during crystallization serves to remove Cl preferentially to F and concentrate F in the residual melt except at very high (>6.5 wt%) melt F contents.

It is important to note that the statements above are generalized behaviors that may be complicated by the combined effects of temperature and pressure, changes in melt concentration, biotite Fe/Mg, and the timing of exsolution of a compositionally-evolving MVP, as will be described subsequently. In order to disentangle these competing and/or compounding effects, we have developed a model of fractional crystallization with or without MVP loss that takes into account partitioning of F, Cl and OH between the phases involved, and their dependencies on temperature and composition. The model simulates fractional crystallization by considering mass balance of element i at each step, through the relation:

$$C^i_{tot} = X_{solid}C^i_{solid} + X_{melt}C^i_{melt} + X_{fluid}C^i_{fluid} \quad (4)$$

where C^i_{tot}, C^i_{solid}, C^i_{melt} and C^i_{fluid} are the concentrations of component i in the total system, crystallizing solid, melt and fluid, respectively, and X_{solid}, $X_{melt,}$ and X_{fluid} are the individual mass fractions. The model was set up in an Excel spreadsheet, run in increments of X_{melt} of 0.01, and in each subsequent step, C_{tot} was set equal to C_{melt} from the previous step. Only biotite and apatite are assumed to be the halogen-

435 bearing crystallizing phases, in proportions of 2% biotite and 1% apatite (models are insensitive to the
436 choice of these modes, so long as the bulk D is less than 1). Biotite-melt and apatite-melt partition
437 coefficients for F and Cl are taken from Icenhower and London (1997) and Mathez and Webster (2005),
438 with values for biotite of 2 (F) and 5 (Cl), and for apatite of 3 (F) and 1 (Cl). Resulting bulk partition
439 coefficients are 0.07 (F) and 0.11 (Cl). Model Ti concentrations assume a bulk partition coefficient for Ti
440 of 1.5, a value which is required to reproduce the range of biotite Ti concentrations from an initial melt
441 Ti content of 0.11 wt%. Assuming a bulk D >1 that fits the data is consistent with the compatibility of Ti
442 into both biotite and ilmenite (Icenhower and London, 1995; Klemme et al., 2006). The initial melt Ti
443 concentration is constrained from the biotite with the highest Ti content (assumed to be the least
444 evolved), and using a biotite/melt partition coefficient for Ti of 24 (Icenhower and London, 1995). With
445 regards to vapor/melt partitioning, a number of studies have shown that values of $D_{Cl}^{vapor/melt}$ are
446 relatively constant at low Cl concentrations in the melt, but then increase strongly at higher Cl
447 concentrations approaching the coexistence of a vapor + Cl-rich brine, or single phase Cl-rich fluid
448 (Webster and Holloway, 1988; Shinohara et al., 1989; Signorelli and Carroll, 2000). As summarized in
449 Baker and Alletti (2012), the concentration range of constant $D_{Cl}^{vapor/melt}$ for silicic melts is less than ~500
450 μg/g, hence the selection of a constant partition coefficient is appropriate given the low Cl
451 concentrations implied by the SMB biotite compositions (see below). Past work has shown that values
452 of $D_{Cl}^{vapor/melt}$ generally increase with increasing pressure for all melt compositions, but there is
453 significant variation in results, with a range from 0.7 to ~80 reported at 200 MPa, which are the
454 conditions most commonly investigated (summarized in Baker and Alletti, 2012, and Dolejš and Zajacz,
455 2018). As well, it has been shown that in general, values of $D_{Cl}^{vapor/melt}$ decrease with increasing ASI
456 (Metrich and Rutherford, 1992; Webster and De Vivo, 2002). For our calculations, we parameterized the
457 pressure dependence of values for $D_{Cl}^{vapor/melt}$ reported by Webster and Holloway (1988; equation S12 of
458 the Online Material). Those experiments were performed at 200 and 500 MPa and 800-950°C using a
459 peraluminous rhyolite and yield a value of 17 for $D_{Cl}^{vapor/melt}$ at 300 MPa. There is no discernable
460 temperature dependence to this data. Vapor/melt partition coefficients for fluorine do not show the
461 same complexity as for Cl since a F-rich fluid does not form at modest F concentrations in the melt.
462 Experimental results reported by Webster (1990) and Webster and Holloway (1990) involved a
463 peraluminous rhyolite composition with < 2 wt% F at 200 MPa and 775-994°C and yielded values of $D_F^{vapor/melt}$
464 of 0.13 to 0.37, respectively, with a value of 0.3 adopted for the model calculations (see Table 2
465 for a summary of model parameters).

Crystallization is assumed to have occurred at 300 MPa, with the H_2O content of the melt either fixed at 7 wt%, which is the haplogranite solubility limit at this pressure (Holtz et al., 2001), or allowed to evolve from a fluid-undersaturated state (in this case 2 wt%) until saturation is achieved. The initial F content of the melt is estimated to be 600 μg/g, which is a value consistent with biotite compositions from the least evolved (i.e., most Ti-rich, Fe-poor) samples. For comparison, whole-rock F-SiO_2 systematics from the Nova Scotia Department of Resources and Renewables database, yield an average F content of 640 μg/g for samples with less than 70 wt% SiO_2, but with a range of ~400 to 900 μg/g. We are unaware of any compositional data for the chlorine content of SMB samples, but instead estimate an initial Cl concentration of 60 μg/g in the fluid saturated case, and 27 μg/g Cl for an initial water content of 2 wt%, again consistent with the composition of the least evolved biotite samples. This difference in initial Cl content between the two models is because X_{Cl}^{biot} increases as the mole fraction of H_2O in the melt decreases, and it was considered important to compare the X_{Cl}^{biot} compositional trends from a similar starting point. The resulting F/Cl ratio of 10 and 22 estimated for the initial melt composition is consistent with values of $\geq$10 for undifferentiated strongly peraluminous igneous rocks (summarized in Dolejš and Zajacz, 2018). The composition of the coexisting biotite, in terms of mole fractions (X^{biot}) of F, Cl and OH endmembers, at each step is calculated by recasting the melt Cl, F and H_2O abundances into respective mole fractions (X^{melt}) using the approach of Li and Herman (2015), and applying the equilibrium constants (K_D) for the biotite-melt F-Cl-OH exchange:

$$K_D(\text{OH-F}) = (X_{OH}^{biot} * X_F^{melt})/(X_F^{biot} * X_{OH}^{melt}) \quad (5)$$

$$K_D(\text{OH-Cl}) = (X_{OH}^{biot} * X_{Cl}^{melt})/(X_{Cl}^{biot} * X_{OH}^{melt}) \quad (6)$$

derived from the experiments of Icenhower and London (1997; see the Online Material for details). The resulting parameterizations for K_D include a dependence on $X_{Fe}^{biotite}$ and temperature (equations S10 and S11 in the Online Material). The change in biotite composition during crystallization was parameterized from the observed $X_{Fe}^{biotite}$-Ti variation in the SMB dataset. Temperature was incorporated into the model by assuming a linear decrease with decreasing melt fraction, with initial (780°C) and final (660°C) values consistent with those predicted by MELTS to produce the observed range in biotite Fe#-Ti abundances.

We investigated two crystallization scenarios. In the first, a free MVP phase is present at each crystallization step, with the amount of vapor set equal to that produced by solidifying a given mass of melt, with all the water in that solidified melt increment expelled into the vapor. The amount of vapor

produced will therefore be dictated by the water solubility, which remains fixed at 7 wt% throughout the model. In the second model, melt is initially vapor undersaturated, allowing the water content to build up due to the crystallization of a predominantly anhydrous assemblage (bulk $D_{H2O} = 0$) until the solubility limit of 7 wt% is achieved, after which the melt evolution proceeds as per the water saturated model. Results for the models are compared to the F-Cl-OH vs Ti trends and the OH/10-Cl*10-F ternary relations in Figures 8a and b, respectively. Figure 8c tracks the variation in the Cl and F abundances in melt and vapor as a function of the fraction of melt remaining. In general, the models reproduce the relative F, Cl and OH compositions of the SMB biotite, in that the OH endmember predominates over the F and Cl endmembers. The models also reproduce the trends of decreasing OH- with decreasing Ti exhibited by the SMB dataset. F and Cl exhibit somewhat different behavior depending on the presence of a MVP or not. Crystallization in the presence of a MVP results in a continuous decrease in the melt and MVP Cl content and $X_{Cl}^{biotite}$, and increase in melt and MVP F content and $X_{F}^{biotite}$. The melt F concentration shows similar behavior in the absence of a MVP, whereas melt Cl increases, to the point of MVP saturation, then decreases. For the MVP undersaturated case, $X_{F}^{biotite}$ and $X_{Cl}^{biotite}$ decrease, although the latter at a slower rate than in the presence of a MVP. These decreases in $X_{F}^{biotite}$ and $X_{Cl}^{biotite}$ are both opposite to the increases in F and Cl concentrations in the melt, and reflect the combined effects of falling temperature and increasing $X_{Fe}^{biotite}$ on the biotite-melt K_D. The continuous decrease in $X_{Cl}^{biotite}$ with biotite Ti concentration exhibited by the SMB data is generally consistent with either crystallization model, given the scatter to the data, and that the limitation of our sampling only allows for a partial crystallization history to be recorded for most plutons. However, the initial decrease in $X_{F}^{biotite}$ predicted by the fluid undersaturated model seems generally inconsistent with the trends in the data, which is most clearly depicted on the OH/10-Cl*10-F ternary (Figure 8b). We therefore suggest that the global trends in F-Cl-OH exhibited by the SMB biotite are most consistent with the incremental removal of a MVP as crystallization proceeds. In this respect, our previously defined trends 1 and 2 reflect different segments of a continuum of vapor-saturated crystallization. In support of the evidence for a MVP from biotite compositions, Clarke et al. (2013) have documented field evidence for crystallization under vapor-saturated conditions at least for some portions of the SMB. In their study of the stage 2 Halifax pluton, Clarke et al. (2013) describe meter-scale, cylindrical ring schlieren which occur as alternating melanocratic gradational to leucocratic bands, interpreted as the trace of gas bubbles migrating through a partially crystalline matrix. Other evidence for vapor saturation includes miarolitic cavities at the core of some ring schlieren, and their association with pegmatitic xenolith breccia pipes.

Figure 8c portrays the results of the crystallization models and also includes a comparison with previous measurements of the Cl abundances considered to be of primary origin from mineral deposits associated with the Stage 1 Salmon Tail, and Stage 2 Davis Lake and New Ross plutons. For the model case of initial MVP saturation, Cl abundances in the vapor decrease throughout crystallization, whereas at the point of vapor saturation in the initially undersaturated case, the MVP abundance of Cl is initially elevated, then decreases with further crystallization. Both of these results are due to the strong sequestration of Cl into the vapor phase, which is subsequently removed and isolated from the crystallizing system. Whereas the model predicts a relatively low Cl primary MVP (250 to 1500 μg/g Cl), the inferred primary orthomagmatic MVP from the SMB mineralised samples have at least 100-fold higher Cl abundances. It is not completely clear why this difference exists. The strong depletion in the Cl content of SMB biotites is a clear indication of growth from low Cl melts. There is the possibility of post-magmatic halogen exchange, resetting the primary mineral abundances, although this would have to be pervasive to the entire SMB dataset. Alternatively, the natural fluid compositions may reflect more extreme levels of crystallization in which fluid saturation was supressed. In contrast to chlorine, fluorine continuously increases in concentration in the melt because $D^{vapour/melt} < 1$. For comparison in Figure 8c is the fluorite solubility data reported by Icenhower and London (1997) involving a peralumnious rhyolite composition in experiments done at 200 MPa and 640-680°C. Reported solubilities range from 8,300 to 18,000 μg/g, with model fluorine concentrations in the melt approaching the lower end of this range with ~6% liquid remaining. The model would therefore predict fluorite to be a late-forming phase in the SMB, which is consistent with the presence of interstitial fluorite in more evolved rock-types, as well as in associated greisens and hydrothermal veins (Muecke and Clarke, 1981).

As a final point, there are several sample groups that deviate significantly from the magmatic F-Cl-OH trends, including the most Ti-poor biotite compositions (<0.5 wt%) with higher Cl and lower F, samples with 0.5 to 1 wt% Ti that are unusually F-rich and Cl-poor and a group at 1.5 wt% Ti that are both Cl- and F-rich (Figure 8a). Nearly all of the samples that show this behavior are of the low Nb/Ta type, previously ascribed to formation by fluid-mediated processes (Dostal and Chatterjee, 2000). The calculated variation in MVP compositions shown in Figure 8c indicates that as crystallization proceeds, fluorine becomes progressively more enriched in the MVP, and chlorine more depleted, with the F/Cl evolving from ~0.2 to ~20 as F varies from 1 to 0.3 for the case of initial fluid saturation. We speculate that the anomalous group of samples with high F and low Cl in the range of 0.5 to 1 wt% Ti might

559 represent equilibration with such high F, low Cl fluids produced during the late stages of crystallization.
560 Origins of the other anomalous subgroups are less clear and subject to further study.

561 To summarize the interpretation of halogen behavior. Both F and Cl are expected to be
562 incompatible in the SMB crystallizing assemblage, and therefore build up in the residual melt, which
563 would be reflected by increasing F and Cl in biotite with indices of differentiation. Although F increases
564 in the expected manner, Cl becomes more depleted in later-crystallized biotite. Model calculations
565 support the hypothesis that the observed behaviour is the result of crystallization under vapour
566 saturated conditions, which is consistent with some field indications of the presence of a MVP. The
567 composition of both the melt and MVP are expected to become more F-rich and Cl-poor as
568 crystallization proceeds; model F enrichment after extensive crystallization is consistent with modal
569 fluorite in some SMB samples and the interaction of high F/Cl fluids may explain some of the anomalous
570 biotite compositions in SMB samples with low Nb/Ta.

571 **5.3 Oxygen fugacity of the SMB**

572 The relatively reduced nature of the SMB, as documented by the biotite compositional
573 systematics, is similar to other peraluminous volcanic and plutonic rock associations. For example,
574 Pichavant et al. (1988) estimated fO_2 of FMQ-2 to FMQ for samples of the Pliocene-Miocene Macusani
575 volcanics (SE Peru), similar to values of <FMQ for Precambrian peraluminous granites reported by
576 Bucholz et al. (2018), as well as High Himalayan leucogranites (Scaillet et al., 1995). In their study of
577 plutons comprising the Mesozoic California Batholith (USA), Ague and Brimhall (1988) showed that the
578 more reduced granites tend to be peraluminous (so-called I-type, strongly contaminated; I-SCR),
579 recording fO_2 of ~FMQ to FMQ-2, compared to the systematically higher values of FMQ-1 to FMQ+2 for
580 subaluminous compositions. Similarly, Lalonde and Bernard (1993) estimated the fO_2 of the Bishop and
581 Hepburn plutonic suites from the Proterozoic Wopmay orogen (NWT, Canada), with the dominantly
582 peraluminous Hepburn suite recording fO_2 of ~FMQ, in contrast to the Bishop suite, whose compositions
583 are mostly subaluminous, and more oxidized at ~FMQ + 2. Whalen and Chappell (1988) have
584 summarised the opaque and mafic mineral characteristics of Silurian to Devonian granites intruded into
585 the Lachlan fold belt (Australia), with results indicating that most ilmenite-bearing peraluminous
586 granites (so-called S-type; Chappell and White, 2001) formed at fO_2 of <FMQ, although some magnetite-
587 bearing S-type granites may reflect conditions ~FMQ. Based on the presence of magnetite, and other
588 indicators, associated subaluminous granites are estimated to have formed at fO_2 >FMQ.

In all of the aforementioned cases, the origin of the overall reduced nature of peraluminous plutonic or volcanic suites is considered to be either a characteristic inherited from the granite source, and/or from processes occurring during magma differentiation, with a paramount role for carbon as a reducing agent. The origin of the carbon is from the sediment protoliths that comprise the magma source (Chappell and White, 2001; Pichavant et al., 1988; Scaillet et al 1995) or is a component of the sediment-derived contaminants assimilated during magma ascent and emplacement (Ague and Brimhall, 1988). The magma redox state imposed by the presence of carbon can be estimated from the stability of graphite coexisting with a C-O or C-O-H fluid, which at 700°C, ranges from FMQ to FMQ-1 (C-O fluid) and FMQ-1 to FMQ-1.5 (C-O-H fluid) at pressures of 200-500 MPa (Bucholz et al., 2018). Such values are consistent with the ranges recorded by other peraluminous suites as described above. Redox evolution to a more oxidized state may occur through several processes, including: 1) eventual loss of graphite during melting/assimilation and the potential role of magma oxidants, such as sedimentary sulfate (Bucholz et al., 2018), 2) the removal of ferrous iron by mineral crystallization or brine exsolution (Carmichael, 1991; Bell and Simon, 2011) or 3) loss of hydrogen (as H_2, H_2S or HCl) during decompression and fluid exsolution (Burgisser and Scaillet, 2007; Candela, 1986). Geochemical and petrographic information from SMB samples is consistent with graphite playing a role in controlling magma redox state. Sr-Nd-Pb-Hf isotopic evidence indicates that SMB magmas are in part formed by melting or assimilation of so-called Tangier felsic crust considered to be Avalon zone basement rocks (Erbez et al., 1991; Dostal et al., 2004; Dostal and Chatteree, 2010; Bickerton et al., 2022). The proposed felsic crust is represented by Group A felsic granulite facies xenoliths, containing abundant graphite (Owen et al., 1988), which occur in late-Devonian mafic intrusive bodies cross-cutting the SMB and surrounding lithologies (Tate and Clarke, 1995). There is also abundant petrographic (e.g., Clarke, 2007; Clarke and Carruzzo, 2007; Clarke et al., 2009; Erdmann et al., 2009), isotopic and geochemical evidence (Clarke et al., 2004; Shelnutt and Dostal, 2012) for assimilation of graphite-bearing wall-rock comprised of metamorphosed graywackes and shales of the Cambro-Ordovician Meguma Group (Hilchie and Jamieson, 2014).

As mentioned in section 4.3.2, some of the more evolved (high Fe#, low Ti) biotite compositions from Stage 2 plutons cross the MELTS model curves suggesting equilibration at fO_2 of FMQ and above. This is also the case for the less evolved samples from the Stage 1 Five Mile Lake pluton. Other evidence for an increase in fO_2 in the late stages of SMB differentiation comes from the composition of the magma-derived fluids responsible for greisen formation associated with the Davis Lake pluton (East Kemptville Sn deposit). In this case, calculated fO_2 is the range of FMQ to FMQ + 0.5 based on inclusion

621 CO_2/CH_4 ratios (Halter et al., 1995). Previous studies have also documented evidence for magma
622 oxidation attending granite differentiation, for example in the Finnmarka Complex (Norway; Czamanske
623 and Wones, 1973) and the High Himalayan Gangotri leucogranites (Scaillet et al., 1995), attributed to
624 magma degassing and hydrogen loss as the mechanism. Further verification of the SMB oxidation
625 trends will require more detailed studies of the individual plutons.

626 **6.0 Implications for element enrichment processes in the South Mountain Batholith**

627 The approach taken in this study is to compare the compositional variation in biotite to
628 crystallization models to track both the redox state of the SMB-forming magmas, the timing of vapor
629 saturation and estimates of the melt and vapor halogen content. This information has implications for
630 understanding the behaviour of redox-sensitive elements in terms of likely enrichment processes
631 leading to ore formation. Important considerations in this context are mineral solubility and crystal-melt
632 partitioning, the magnitude of MVP-melt partitioning, and element complexing in the vapor phase, as
633 described below.

634 The granophile suite of elements considered to be redox sensitive are those for which there is
635 evidence for the presence of multiple oxidation states in silicate melts over the range in fO_2 of terrestrial
636 magmas. These include Sn (2+, 4+), U (4+, 6+), Mo (4+, 6+) and W (4+, 6+) (Calas, 1979; Farges et al.,
637 2006a, b; Linnen et al., 1995; 1996; Fonseca et al., 2014). In terms of related ore-forming minerals, the
638 solubility of SnO_2 (cassiterite) and UO_2 (uraninite) in both silicate melt and MVP have been shown to
639 vary with fO_2. SnO_2 becomes more soluble in both melt and MVP with decreasing fO_2 (Linnen et al.,
640 1995; 1996; Taylor and Wall, 1993), whereas UO_2 shows the opposite behaviour (Peiffert et al., 1994;
641 1996). Reducing conditions will serve to suppress saturation in SnO_2, maintaining Sn as a dissolved
642 component during crystallization. At fO_2 of ~FMQ and below, Sn^{2+} is the predominant melt species in
643 peraluminous melt compositions (Linnen et al., 1996; Farges et al., 2006a), with an estimated ionic
644 radius of 111 pm in VI-fold coordination (Uchida et al., 2002). Divalent Sn is therefore a poor fit for
645 isovalent substitution into the major Mg^{2+} (IR = 72 pm), Fe^{2+} (IR = 78 pm) or Ca^{2+} (IR = 100 pm; Shannon,
646 1976) sites in dominant rock-forming silicates, contributing to a concentration buildup of Sn in the melt
647 as crystallization proceeds. Both of these effects mean that more reducing conditions enhance the
648 favourability of high Sn concentrations in residual melts and minerals as being available to a MVP for
649 sequestration. Although UO_2 becomes less soluble with decreasing fO_2 (Peiffert et al., 1994; 1996),
650 suggesting early precipitation might be a barrier to buildup during crystallization, Peiffert et al. (1996)
651 document an extraordinarily strong melt composition control on solubility, with peraluminous melts

652 dissolving >100 fold higher U concentrations than peralkaline compositions. The fO_2 dependence on
653 solubility is also diminished in peraluminous compositions (Peiffert et al., 1996). Hence, the melt
654 composition control on solubility, combined with the fact that U^{4+}, which is expected to be the dominant
655 species at the reduced conditions of the SMB-forming magma (Calas, 1979; Farges et al., 1992), is also a
656 poor fit into major crystallizing phases (IR = 89 pm; Shannon, 1976), may still allow for significant
657 enrichment by crystallization. Highly charged cations, such as W^{4+} and Mo^{4+} have ionic radii in VI-fold
658 coordination (66 and 65 pm, respectively; Shannon, 1976) similar to Ti^{4+} (61 pm; Shannon, 1976), but
659 their substitution as the 4+ valence state into Ti-bearing phases, such as ilmenite, from non-tetravalent
660 melt species (i.e., W^{6+}, Mo^{6+}) requires exchange reactions involving oxygen (Candela and Bouton, 1990).
661 The combined influences of changing valence state, and non-isovalent exchange can act in opposition,
662 resulting in fractionation between W and Mo, with the relative D^W/D^{Mo} increasing with fO_2 (Candela and
663 Bouton, 1990). Provided that these mechanisms control the substitution of W and Mo for Ti in all the
664 crystallizing ferromagnesian phases (e.g., ilmenite and biotite), there will be a resulting increase in
665 W/Mo in the melt with decreasing fO_2 (Candela and Bouton, 1990). This effect will increase the
666 availability of W relative to Mo for extraction by a MVP. The overall implication is that Sn, and perhaps
667 W (by virtue of the fO_2-shift in mineral/melt D^W/D^{Mo}), are the granophile ore elements for which a
668 causative link can be made between the potential for mineralization by element buildup during
669 crystallization and the overall reduced nature of the SMB. Evidence for a redox shift to more oxidizing
670 conditions, such as lower biotite Fe# at a given Ti concentration compared to the trends indicated in
671 Figure 9, would suggest conditions conducive to Sn deposition owing to a shift to less soluble behaviour
672 in melt and MVP.

673 Limited data are available to evaluate the role of fO_2 in affecting MVP/melt partitioning for the
674 above-described suite of elements. Results documented for U over the fO_2 range of FMQ to FMQ +10
675 indicate that $D_U^{MVP/melt}$ increases only 10-fold or less for experiments with either NaCl- (0.08-4.4 m) or
676 NaF- (0.02-0.22 m) bearing aqueous fluids (Peiffert et al., 1994; 1996). Tattich and Blundy (2017)
677 documented a ~3-fold increase in $D_{Mo}^{MVP/melt}$ from ~FMQ+1 to ~FMQ+3 for experiments containing NaCl-
678 bearing fluids done at 200 MPa and 725°C. Values of $D_{Sn}^{MVP/melt}$ have not been measured as a function of
679 fO_2, but comparison of the change in solubility of SnO_2 in silicate melt (Linnen et al., 1995; 1996) versus
680 MVP (Taylor and Wall, 1993) as a function of fO_2 suggests the decrease in solubility into the melt is
681 greater than into the vapour, with the difference increasing with increasing HCl molality in the vapour
682 (Taylor and Wall, 1993). Therefore, similar to U and Mo, $D_{Sn}^{MVP/melt}$ is estimated to show a small increase
683 with increasing fO_2. This is also supported by empirical measurements of $D_{Sn}^{MVP/melt}$ from natural suites

equilibrated at different fO_2 (Zajacz et al., 2008). Like Sn, $D_W^{MVP/melt}$ has not been measured as a function of fO_2. However, tungstate mineral solubility in peraluminous melts shows negligible fO_2 dependence over the range of ~FMQ-2 to FMQ+3 (Che et al., 2013). Therefore, more reduced conditions would tend to favour the partitioning of Sn, U and Mo into the melt rather than the vapor phase, and enhance the effect of crystallization buildup on enrichment of the residual melt.

There are somewhat conflicting results in terms of the magnitude of $D^{MVP/melt}$ for Sn, U, Mo, and W, and the importance of complexing agents such as Cl and F. For example, some experimental studies pertaining to upper crustal P-T conditions (e.g., 100-200 MPa, 750-850°C) suggest that W (Bai and Koster Van Groos, 1999) and Sn (Keppler and Wyllie, 1991; Hu et al, 2008) will be more strongly partitioned into the melt, with $D^{MVP/melt}$ in the range of 10^{-4} to 0.5, although results from the same studies suggest that complexing with chloride could be important for both elements. Other studies, including those that measured trapped fluid inclusions in quenched run products, have reported that W (Manning and Henderson, 1984; Keppler and Wyllie, 1991; Schafer et al., 1999; Schmidt et al., 2020), Sn (Schmidt et al., 2020; Zhao et al., 2022), and Mo (Candela and Holland, 1984; Keppler and Wyllie, 1991; Schafer et al., 1999; Tattiche and Blundy, 2017; Jiang et al., 2021) are fluid compatible, with $D^{MVP/melt}$ ranging from ~1 to 35, with evidence for chloride complexing of Sn and Mo. The fluid compatible behavior of W, Sn and Mo is also supported by measurements of coexisting melt and fluid inclusions from natural magmatic suites (Zajacz et al., 2008; Audétat et al., 2000; Audétat et al., 2008; Audétat, 2019), with evidence for chloride complexing of W and Sn. In contrast to Cl, few studies provide evidence for fluoride complexing of granophile metals. Values for $D^{MVP/melt}$ for both Sn and W do not change as a function of the F content of a vapor-melt system or may decrease slightly with increasing F concentration (Manning and Henderson, 1984, Keppler and Wyllie, 1991). All previous experimental studies of MVP/melt partitioning of U report strong compatibility in the melt phase, with evidence for both Cl and F complexing (Keppler and Wyllie, 1991; Pfieffert et al., 1994).

The impact on metal sequestration in the SMB of a continuously exsolving MVP under reducing conditions can therefore be summarized as follows. First, low fO_2 during crystallization affects the solubility and mineral/melt partitioning of the redox-sensitive elements Sn, W, U and Mo, serving to suppress early SnO_2 precipitation, and cause both an increase in W/Mo and an overall buildup of all four elements in evolving SMB liquids. Second, available experimental data indicate that reducing conditions also shifts $D^{MVP/melt}$ to favor partitioning into the melt phase. Third, as the calculated chlorine and fluorine contents of the MVP will decrease and increase, respectively, as SMB crystallization proceeds

(Figure 8c), this suggests that the extraction efficiency for Cl-complexed metals will decline, with increased fluorine possibly magnifying this effect for Sn and W. Results of numerical models (e.g. Audetat, 2019) also show that progressively larger values of $D^{MVP/melt}$ are required to deplete the melt in a particular element as vapor exsolution occurs earlier during crystallization. Therefore, early vapor exsolution under reducing conditions also lessens the extraction efficiency of these redox-sensitive elements to the MVP. All of these aspects would favor extreme levels of crystallization as the most effective means of metal concentration for the redox-sensitive metals consider here.

Acknowledgements

This research was supported through the Mineral Resources Development Fund of the Nova Scotia Department of Resources and Renewables, and NSERC Discovery Grants to JB and JH. We are grateful to Mick O'Neill for access to the Nova Scotia Department of Energy and Mines Drill Core Library at Stellarton. Thanks to Fergus Tweedale for offering his expertise and assistance in sample acquisition and his general knowledge of the SMB, and to Mitch Kerr for his expertise in thin section preparation and providing a rapid turnaround when time was tight. Dalhousie undergraduates Rosa Toutah and Natalie Shields helped with the laser ablation and electron microprobe analyses. Barrie Clarke is thanked for providing an informal review of the manuscript. We appreciate the comments from the American Mineralogist anonymous reviewer and Dave Lentz, which improved the clarity of the manuscript.

References cited

Ague, J. J. and Brimhall, G. H. (1988) Regional variations in bulk chemistry, mineralogy, and the compositions of mafic and accessory minerals in the batholiths of California. Geological Society of America Bulletin 100, 891–911.

Audetat, A. (2019) The metal content of magmatic-hydrothermal fluids and its relationship to mineralization potential. Economic Geology, vol 114, pp 1033-1056.

Audetat, A., and Pettke, T. (2003) The magmatic-hydrothermal evolution of two barren granites: A melt and fluid inclusion study of the Rito del Medio and Canada Pinabete plutons in northern New Mexico (USA): Geochimica et Cosmochimica Acta, v. 67, p 97-121.

Audétat, A., Pettke, T., Heinrich, C.A., and Bodnar, R.J. (2008) The composition of magmatic-hydrothermal fluids in barren and mineralized intrusions. Economic Geology, v. 103, p. 877–908.

Azadbakht, Z., Lentz, D.R., McFarlane, C.R.M., and Whalen, J.B. (2020) Using magmatic biotite chemistry to differentiate barren and mineralized Silurian–Devonian granitoids of New Brunswick, Canada. Contributions to Mineralogy and Petrology, 175:69.

Baker, D.R. and Alletti, M. (2012) Fluid saturation and volatile partitioning between melts and hydrous fluids in crustal magmatic systems: The contribution of experimental measurements and solubility models. Earth-Science Reviews, vol 114, pp 298-324.

Bailey, S.W. (1984) Classification and structures of the micas. In Micas, Reviews in Mineralogy, Mineralogical Society of America, pp. 1-14.

Ballouard C., Massuyeaua, M., Elburga, M.A., Tappea, S., Viljoena, F., and Brandenburget, J-F. (2020) The magmatic and magmatic-hydrothermal evolution of felsic igneous rocks as seen through Nb-Ta geochemical fractionation, with implications for the origins of rare-metal mineralizations. Earth Science Reviews, vol 203, pp 1-31.

Ballouard, C., Poujol, M., Boulvais, P., Branquet, Y., Tartese, R., and Vigneresse, J.L. (2016) Nb-Ta fractionation in peraluminous granites: A marker of the magmatic-hydrothermal transition. Geology, vol 44, pp 231-234.

Bai, T.B. and A.F. Koster Van Groos (1999) The distribution of Na, K, Rb, Sr, Al, Ge, Cu, W, Mo, La, and Ce between granitic melts and coexisting aqueous fluids. Geochimica et Cosmochimica Acta, vol. 63, pp. 1117–1131.

Bali E., Keppler, H., and Audétat, A. (2012) The solubility of W and Mo in subduction zone fluids and the Mo-W-Th-U systematics of island arc magmas. Earth and Planetary Science Letters, vol 351, pp 195-207.

Bell A.S. and Simon, A. (2001) Experimental evidence for the alteration of the $Fe^{3+}/\Sigma Fe$ of silicate melt caused by the degassing of chlorine-bearing aqueous volatiles. Geology, vol 39, pp.499-502.

Bennett, V.W. (1990) Mineralogy and Chemistry of Biotite and Muscovite from the Granitoid Rocks of the Bay d'Espoir Area, Newfoundland. B.Sc. thesis, Memorial University, St. John's, Newfoundland.

Berni, G.V., Wagner, T., Fusswinkel, T., and Wenzel, T. (2017) Magmatic-hydrothermal evolution of the Kymi topaz granite stock, SE Finland: Mineral chemistry evidence for episodic fluid exsolution. Lithos, vol 292-293, pp 401-423.

Bickerton, L., Kontak, D.J., Murphy, B., Kellett, D.A., Samson, I.M., Marsh, J., Dunning, G.R., and Stern, R.A. (2022) The age and origin of the South Mountain Batholith (Nova Scotia, Canada) as constrained by zircon U-Pb geochronology, geochemistry and O-Hf isotopes. Canadian Journal of Earth Sciences, vol 59, pp. 418-454.

Bogaerts, M., Scaillet, B., and Auwera, J. V. (2006) Phase equilibria of the Lyngdal granodiorite (Norway): implications for the origin of metaluminous ferroan granitoids. Journal of Petrology vol 47, 2405–2431.

Bucholz, C.E., Stolper, E.M., Eiler, J.M., and Breaks, E.W. (2018) A Comparison of Oxygen Fugacities of Strongly Peraluminous Granites across the Archean– Proterozoic Boundary. Journal of Petrology, vol 59, pp 2123-2156.

Burgisser A. and Scaillet, B. (2007) Redox evolution of a degassing magma rising to the surface. Nature, vol 445, pp 194-197.

Calas, G. (1979) Etude expérimentale du comportement de l'uranium dans les magmas, états d'oxydation et de coordinance. Geochimica et Cosmochimica Acta, vol 43, pp 1521-1531.

Candela P. A. (1986) The evolution of aqueous vapor from silicate melts: Effect on oxygen fugacity. Geochimica et Cosmochimica Acta, vol 50, pp 1205-1211.

786 Candela P.A. and Holland H.D (1984) The partitioning of copper and molybdenum between silicate melts
787 and aqueous fluids. Geochimica et Cosmochimica Acta, vol 48, pp 373-380.

788 Candela P.A. and Holland H.D. (1986) A mass transfer model for copper and molybdenum in magmatic
789 hydrothermal systems; the origin of porphyry-type ore deposits. Economic Geology, vol 81, pp 1-19.

790 Candela, P.A. and Bouton, S.L. (1990) The influence of oxygen fugacity on tungsten and molybdenum
791 partitioning between silicate melts and ilmenite. Economic Geology, vol 85, pp 633-640.

792 Carmichael, I. S. E. (1991) The redox states of basic and silicic magmas: a reflection of their source
793 regions? Contributions to Mineralogy and Petrology vol 106, 129–141.

794 Carroll, M.R. and Rutherford, M.J. (1988) Sulfur speciation in hydrous experimental glasses of varying
795 oxidation state results from measured wavelength shifts of sulfur x-rays. American Mineralogist, vol 73,
796 pp.845-849

797 Carruzzo, S., Kontak, D.J, and Clarke, D.B. (2000) Granite-hosted mineral deposits of the New Ross area,
798 South Mountain Batholith, Nova Scotia, Canada: P, T and X constraints of fluids using fluid inclusion
799 thermometry and decrepitate analysis. Transactions of the Royal Society of Edinburgh-Earth Sciences,
800 vol 91 , pp. 303-319.

801 Carruzzo, S., Kontak, D.J, Clarke, D.B., and Kyser, T.K. (2004) An integrated fluid-mineral stable-isotope
802 study of the granite-hosted mineral deposits of the New Ross area, South Mountain Batholith, Nova
803 Scotia, Canada: Evidence for multiple reservoirs. Canadian Mineralogist, vol 42 , pp.1425-1441

804 Chambers, J.A. and Kohn, M.J. (2012) Titanium in muscovite, biotite and hornblende: Modelling,
805 thermometry and rutile activities of metapelites and amphibolites. American Mineralogist, v. 92, p 543-
806 555

807 Chappell, B.W. and White, A.J.R. (2001) Two contrasting granite types: 25 years later. Australian Journal
808 of Earth Sciences vol 48, 489–499.

809 Chavez, J. (2018) Redox state of the South Mountain Batholith: A reconnaissance study using zircon
810 geochemistry. B.Sc. thesis, Dalhousie University, 61 pp.

811 Che, X.D., Linnen, R.L., Wang, R.U., Aseri, A., and Thibault, Y. (2013) Tungsten solubility in evolved
812 granitic melts: An evaluation of magmatic wolframite. Geochimica et Cosmochimica Acta, vol 106, pp
813 84-98.

814 Clarke, D.B. (1981) The mineralogy of peraluminous granites: A review. Canadian Mineralogist, vol 19,
815 pp 3-17.

816 Clarke, D. B. (2007). Assimilation of xenocrysts in granitic magmas; principles, processes, proxies, and
817 problems. Canadian Mineralogist, vol 45, pp 5-30.

818 Clarke, D.B. and Bogutyn, P.A. (2003) Oscillatory epitactic growth zoning in biotite and muscovite from
819 the Lake Lewis leucogranite, South Mountain Batholith, Nova Scotia, Canada. Canadian Mineralogist, vol
820 41, 1027–1047.

821 Clarke, D.B., McKenzie, C.B., Muecke, G.K., and Richardson, S.W. (1976): Magmatic andalusite from the
822 South Mountain batholith, Nova Scotia. Contributions to Mineralogy and Petrology, vol 56, pp 279-287.

Clarke, D.B., Grujic, D., McCuish, K.L., Sykes, J.C.P., and Tweedale, F.M. (2013) Ring schlieren: Description and interpretation of field relations in the Halifax Pluton, South Mountain Batholith, Nova Scotia. Journal of Structural Geology, vol 51, pp 193-205.

Clarke, D. B. and Carruzzo, S. (2007) Assimilation of country-rock ilmenite and rutile in the South Mountain Batholith, Nova Scotia, Canada. Canadian Mineralogist vol 45, pp 31-42.

Clarke, D.B., Fallon, R., and Heaman, L.M. (2000) Interaction among upper crustal, lower crustal, and mantle materials in the Port Mouton pluton, Meguma Lithotectonic Zone, southwest Nova Scotia. Canadian Journal of Earth Sciences, vol 37, pp 579–600.

Clarke, D.B., MacDonald, M.A., and Erdmann, S. (2004) Chemical variation in Al_2O_3–CaO–Na_2O–K_2O space: controls on the peraluminosity of the South Mountain Batholith. Canadian Journal of Earth Sciences, vol 41, pp 785–798.

Clarke, D.B., Erdmann, S., Samson, H., and Jamieson, R.A. (2009) Contamination of the South Mountain Batholith by sulfides from the country rocks. Canadian Mineralogist, vol 47, pp 1159-1176.

Clarke, D.B., Renno, A.D., Hamilton, D.C., Gilbricht, S., Bachmann, K. (2021) The spatial association of accessory minerals with biotite in the granitic rocks from the South Mountain Batholith, Nova Scotia, Canada. Geosphere, vol 18, pp 1-18.

Cline, J.S. and Bodnar, R.J. (1991) Can economic porphyry copper mineralization be generated by a typical calc-alkaline melt? Journal of Geophysical Research, vol 96, pp 8113-8126.

Costa, F., Scaillet, B., and Pichavant, M. (2004) Petrological and experimental constraints on the pre-eruption conditions of Holocene dacite from Volcan San Pedro (36°S, Chilean Andes) and the importance of sulphur in silicic subduction related magmas. Journal of Petrology, vol 45, pp. 855–881.

Czamanske, G. K. and Wones, D. R. (1973) Oxidation during magmatic differentiation, Finnmarka Complex, Oslo Area, Norway: Part 2, the mafic silicates. Journal of Petrology, vol 14, pp. 349–380.

Dall'Agnol, R., Scaillet, B. and Pichavant, M. (1999) An experimental study of a lower Proterozoic A-type granite from the eastern Amazonian Craton, Brazil. Journal of Petrology, vol 40, pp 1673–1698.

Dalou C., Koga K.T., Shimizu N., Boulon J., and Devidal J.-L. (2012) Experimental determination of F and Cl partitioning between lherzolite and basaltic melt. Contributions to Mineralogy and Petrology, vol 163, pp 591–609.

de Albuquerque, C.A.R. (1979) Origin of the plutonic mafic rocks of southern Nova Scotia. Geological Society of America Bulletin vol 90, pp 719–31.

Dolejš, D. and Zajacz, Z. (2018) Halogens in silicic magmas and their hydrothermal systems: In (Harlov, D.E., and Aranovich, L.) The Role of Halogens in Terrestrial and Extraterrestrial Geochemical Processes. Springer. p. 431-543.

Douma, S. (1988) The Mineralogy, Petrology and Geochemistry of the Port Mouton Pluton, Nova Scotia, Canada. Unpublished M.Sc. thesis, Dalhousie University, 345 pp.

Dostal, J. and Chatterjee, A.K. (2000) Contrasting behavior of Nb/Ta and Zr/Hf ratios in a peraluminous granitic pluton (Nova Scotia, Canada). Chemical Geology, vol 163, pp 207–218.

Dostal, J. and Chatterjee, A.K. (2010) Lead isotope and trace element composition of K-feldspars from peraluminous granitoids of the Late Devonian South Mountain Batholith (Nova Scotia, Canada): implications for petrogenesis and tectonic reconstruction. Contributions to Mineralogy and Petrology, vol 159, pp 563–578.

Dostal, J., Chatterjee, A. K., and Kontak, D. J. (2004) Chemical and isotopic (Pb, Sr) zonation in a peraluminous granite pluton: role of fluid fractionation. Contributions to Mineralogy and Petrology, vol 147, pp. 74-90.

Eberz, G.W., Clarke, D.B., Chatterjee, A.K., and Giles, P.S. (1991) Chemical and isotopic composition of the lower crust beneath the Meguma lithotectonic zone, Nova Scotia: evidence from granulite facies xenoliths. Contributions to Mineralogy and Petrology, vol 109, pp 69-88.

Erdmann, S.A., Jamieson, R.A., and MacDonald, M.A. (2009) Evaluating the Origin of Garnet, Cordierite, and Biotite in Granitic Rocks: a Case Study from the South Mountain Batholith, Nova Scotia. Journal of Petrology vol 8, pp 1477-1503.

Eugster H.P. and Wones D.R. (1962) Stability relations of the ferruginous biotite, annite. Journal of Petrology, vol 3, pp. 81-125.

Farges, F. Ponader, C.W., Calas, G,. and Brown, G.E. (1992) Structural environments of incompatible elements in silicate glass/melt systems: II. U^{IV}, U^{V}, and U^{VI}, Geochimica et Cosmochimica Acta, vol 56, pp 4205 – 4220.

Farges, F., Linnen, R.L., and Brown, G.E. (2006a) Redox and speciation of tin in hydrous silicate glasses: A comparison with Nb, Ta, Mo and W. Canadian Mineralogist, vol 44, pp 795-810.

Farges, F., Siewert, R., Ponader, C.W., Brown, G.E., Pichavant, M., and Behrens, H. (2006b) Structural environments around molybdenum in silicate glasses and melts. II. Effect of temperature, pressure, H_2O, halogens and sulfur. Canadian Mineralogist, vol 44, pp 755-773.

Fisher, B.E. (2006) DP ME 37, version 2, digital version of Nova Scotia Department of Natural Resources Map ME 1994-1, geological map of the South Mountain Batholith, western Nova Scotia, scale 1:250 000, by M.A. MacDonald; Nova Scotia Department of Natural Resources, Digital Product DP ME 37.

Fonseca, R.O.C., Mallmann, G., Sprung P., Sommer J.E., Heuser, A., Speelmanns I.M., and Blanchard, H. (2014) Redox controls on tungsten and uranium crystal/silicate melt partitioning and implications for the U/W and Th/W ratio of the lunar mantle. Earth and Planetary Science Letters, vol 404, pp 1–13.

Groves, D.I. (1972) The geochemical evolution of tin-bearing granitic rocks in the Blue Tier Batholith, Tasmania. Economic Geology, vol 67, pp 445–457.

Halter, W.E. and Williams-Jones, A.E. (1999) Application of topaz-muscovite F-OH exchange as a geothermometer. Economic Geology, vol. 94, pp. 1249-1258.

Halter, W.E., Williams-Jones, A.E., and Kontak, D.J. (1996) The role of greisenization in cassiterite precipitation at the East Kemptville tin deposit, Yarmouth County, Nova Scotia. Economic Geology, vol 91, pp 368-385.

Halter, W.E., Williams-Jones, A.E., and Kontak, D.J. (1998) Origin and evolution of the greisenizing fluid at the East Kemptville tin deposit, Nova Scotia, Canada. Economic Geology, vol 93, pp. 1026-1051.

Ham, L.J. (1988) The Mineralogy, Petrology, and Geochemistry of the Halfway Cove-Queensport Pluton, Nova Scotia, Canada. Unpublished M.Sc. thesis, Dalhousie University, 314 pp.

Hauri E.H., Gaetani G.A. and Green T.H. (2006) Partitioning of water during melting of the Earth's upper mantle at H_2O-undersaturated conditions. Earth and Planetary Science Letters vol 248, pp 715–734.

Henry, D., and Guidotti, C. (2002) Titanium in biotite from metapelitic rocks: Temperature effects, crystal-chemical controls, and petrologic applications. American Mineralogist, v. 87, p. 375-382

Henry, D.J., Guidotti, C.V, and Thomson, J.A. (2005) The Ti-saturation surface for low-to-medium pressure metapelitic biotites: Implications for geothermometry and Ti-substitution mechanisms. American Mineralogist, vol 90, pp. 316–328.

Hicks, J.H., Jamieson, R.A., and Reynold, P.H. (1999) Detrital and metamorphic $^{40}Ar/^{39}Ar$ ages from muscovite and wholerock samples, Meguma Supergroup, southern Nova Scotia. Canadian Journal of Earth Sciences, vol 36, pp. 23–32.

Hilchie, L.J. and Jamieson, R.A. (2014) Graphite thermometry in a low-pressure contact aureole, Halifax, Nova Scotia. Lithos, vol 208–209, pp 21–33.

Holtz, F., Behrens, H., Dingwell, D.B., and Johannes, W. (1995) H_2O solubility in haplogranitic melts: compositional, pressure, and temperature dependence. American Mineralogist, vol 80, pp. 94–108.

Hu, X., Bi, X., Hu, R., Shang, L., and Fan, W. (2008) Experimental study on tin partition between granitic silicate melt and coexisting aqueous fluid. Geochemical Journal vol 42, pp 141–150.

Icenhower, J. and London, D. (1995) An experimental study of element partitioning among biotite, muscovite and coexisting peraluminous silicic melt at 200 MPa (H_2O). American Mineralogist, vol 80, pp 1229-1251.

Icenhower, J. and London, D. (1997) Partitioning of fluorine and chlorine between biotite and granitic melt: experimental calibration at 200 Mpa H_2O. Contributions to Mineralogy and Petrology, vol 127, pp 17–29.

Jamieson, R.A., Hart, G.G., Chapman, G.G., and Tobey, N.W. (2012) The contact aureole of the South Mountain Batholith in Halifax, Nova Scotia: Geology, mineral assemblages, and isograds. Canadian Journal of Earth Sciences vol 49, pp. 1280–1296.

Jiang, Z., Shang, L., Guo, H., Wang, X-S, Chen, C. and Zhou, Y. (2021) An experimental investigation into the partition of Mo between aqueous fluids and felsic melts: Implications for the genesis of porphyry Mo ore deposits. Ore Geology Reviews 134 (2021) 104144

Jugo, P.J., Luth, R.W., and Richards, J.P. (2005) Experimental data on the speciation of sulfur as a function of oxygen fugacity in basaltic melts. Geochimica et Cosmochimica Acta, vol 69, pp. 497-503.

Keen, C.E., Kay, W.A., Keppie, D., Marillier, F., Pe-Piper, G., and Waldron, J.W.F. (1991) Deep seismic reflection data from the Bay of Fundy and the Gulf of Maine: tectonic implications for the northern Appalachians. Canadian Journal of Earth Sciences, vol 28, pp 1096–1111.

Keppie, J.D. and Dallmeyer, R.D. (1987) Dating transcurrent terrane accretion: an example from the Meguma and Avalon composite terranes in the northern Appalachians. Tectonics, vol 6, pp. 831–847.

Keppler H. and Wyllie P.J. (1991) Partitioning of Cu, Sn, Mo, W, U and thorium between melts and aqueous fluid in the systems haplogranite-H_2O–HCl and haplogranite-H_2O–HF. Contributions to Mineralogy and Petrology, vol 109, pp. 139– 150.

Klemme, S., Gunther, D., Hametner, K., Prowatke, S. and Zack, T. (2006) The partitioning of trace elements between ilmenite, ulvospinel, armalcolite and silicate melts with implications for the early differentiation of the moon. Chemical Geology vol 234, pp 251–263.

Kontak, D. (1990) The East Kemptville topaz-muscovite leucogranite Nova Scotia 1, Geological setting and whole-rock geochemistry. The Canadian Mineralogist, vol 28, pp 787-825.

Kontak, D.J., Horne, R.J., Sandeman, H., and Archibald, D.A. (1998) $^{40}Ar/^{39}Ar$ dating of whole-rock slates from auriferous veins in the Meguma Group, Nova Scotia: Evidence for post metamorphic timing of vein formation. Canadian Journal of Earth Sciences, vol 35, pp. 746–761.

Lalonde, A. E. and Bernard, P. (1993) Composition and color of biotite from granites: two useful properties in the characterization of plutonic suites from the Hepburn Internal Zone of the Wopmay Orogen, Northwest Territories. Canadian Mineralogist vol 31, pp. 203–217.

Li, J-X., Fan, W.-M., Zhang, L.-Y., Ding, L., Yuea, Y-H., Xiea, J., Caia, F-L., Quan, Q.-Y., Sein, K. (2020) Biotite geochemistry deciphers magma evolution of Sn-bearing granite, southern Myanmar. Ore Geology Reviews, vol 121, 103565.

Linnen R.L., Pichavant, M. and Holtz, F., and Burgess, S. (1995) The effect of fO_2 on the solubility, diffusion, and speciation of tin in haplogranitic melt at 850°C and 2 kbar. Geochimica et Cosmochimica Acta, vol 59, pp 1579-1588.

Linnen R.L., Pichavant, M., and Holtz, F. (1996) The combined effects of fO_2 and melt composition on SnO_2 solubility and tin diffusivity in haplogranitic melts. Geochimica et Cosmochimica Acta, vol 60, pp 4965-4976.

London, D. (1997) Estimating abundances of volatile and other mobile components in evolved silicic melts through mineral–melt equilibria. Journal of Petrology, vol 38, pp 1691-1706.

Ludington, S. (1978) Biotite-apatite geothermometer revisited. American Mineralogist, vol 63, pp.551-553.

MacDonald, M.A. (1981) The Mineralogy, Petrology and Geochemistry of the Musquodoboit Batholith. Unpublished M.Sc. thesis, Dalhousie University, 209 pp.

MacDonald, M.A. (2001) Geology of the South Mountain Batholith, Southwestern Nova Scotia. Nova Scotia Department of Natural Resources, Open File Report ME 2001-2.

Manning, D.A.C. and Henderson, P. (1984) The behavior of tungsten in granitic melt-fluid systems. Contributions to Mineralogy and Petrology, vol 86, pp 286-293.

Mason, R.A. (1992) Models of order and iron-fluorine avoidance in biotite. Canadian Mineralogist vol 30, pp 343-354.

Mathez E. A. and Webster J. D. (2005) Partitioning behavior of chlorine and fluorine in the system apatite–silicate melt–fluid. Geochimica et Cosmochimica Acta, vol 69, pp 1275–1286.

Metrich, N, and Rutherford, M.J. (1992) Experimental study of chlorine behavior in hydrous silicic melts. Geochimica et Cosmochimica Acta, v. 56, p. 607-616.

Muecke, G.K. and Clarke, D.B. (1981) Geochemical evolution of the South Mountain Batholith, Nova Scotia: rare-earth-element evidence. Canadian Mineralogist, vol 19, pp 133-145.

Müller, A., Seltmann, R., Halls, C., Siebel, W., Dulski, P., Jeffries, T., Spratt, J., and Kronz, A. (2006) The magmatic evolution of the Land's End pluton, Cornwall, and associated pre-enrichment of metals. Ore Geology Reviews, v. 28, p 329-367.

Munoz, J.L. (1984) F–OH and Cl–OH exchange in micas with applications to hydrothermal ore deposits. In Micas, Reviews in Mineralogy, Mineralogical Society of America, pp. 469–493

Munoz, J.L. and Ludington, S. (1974). Fluoride-hydroxyl exchange in biotite. American Journal of Science, vol 274, pp 393–413.

Mutch, E. J. F., Blundy, J. D., Tattitch, B. C., Cooper, F. J., and Brooker, R. (2016) An experimental study of amphibole stability in low-pressure granitic magmas and a revised Al-in-hornblende geobarometer. Contributions to Mineralogy and Petrology vol 171, article 85.

Owen, J.V., Greenough, J.D., Hy, C., and Ruffman, A. (1988) Xenoliths in a mafic dyke at Popes Harbour, Nova Scotia: implications for the basement to the Meguma Group. Canadian Journal of Earth Sciences, vol 25, pp 1464-1471.

Patiño Douce, A.E. (1993) Titanium substitution in biotite: an empirical model with applications to thermometry, O_2 and H_2O barometries, and consequences form biotite stability. Chemical Geology, vol 108, pp 133–162.

Peiffert, C., Cuney, M., and Nguyen-Trung, C. (1994) Uranium in granitic magmas: Part 1. Experimental determination of uranium solubility and fluid-melt partition coefficients in the uranium oxide-haplogranite-H_2O-Na_2CO_3 system at 770°C, 2 kbar. Geochimica et Cosmochimica Acta, vol 58, pp 2495-2507.

Peiffert, C., Nguyen-Trung, C., and Cuney, M. (1996) Uranium in granitic magmas: Part 2. Experimental determination of uranium solubility and fluid-melt partition coefficients in the uranium oxide-haplogranite-H_2O-NaX (X = Cl, F) system at 770°C, 2 kbar. Geochimica et Cosmochimica Acta, vol 60, pp 1515-1529.

Pichavant, M., Kontak, D. J., Valencia Herrera, J., and Clark, A. H. (1988) The Miocene–Pliocene Macusani Volcanics, SE Peru. I: Mineralogy and magmatic evolution of a two-mica aluminosilicate-bearing ignimbrite suite. Contributions to Mineralogy and Petrology, vol 100, pp 300–324.

Pirajno, F. (2018) Halogens in hydrothermal fluids and their role in the formation and evolution of hydrothermal mineral systems: In (Harlov, D.E., and Aranovich, L.) The Role of Halogens in Terrestrial and Extraterrestrial Geochemical Processes. Springer. p. 759-804.

Righter, K. and Carmichael, I.S.E. (1996) Phase equilibria of phlogopite lamprophyres from western Mexico: biotite-liquid equilibria and P-T estimates for biotite-bearing igneous rocks. Contributions to Mineralogy and Petrology, vol 123, pp 1-21.

Rubbo, M. and Bruno, M. (2003) Coronitic reactions: constraints to element diffusion during UHP metamorphism. EMU Notes in Mineralogy, v. 5, chp 5., p. 1-209.

Sallet, R. (2000) Fluorine as a tool in the petrogenesis of quartz-bearing magmatic associations: Applications of an improved F–OH biotite–apatite thermometer grid. Lithos, vol 50, pp. 241–253.

Scaillet, B. and Evans, B.W. (1999) The 15 June 1991 eruption of Mount Pinatubo. I. Phase equilibria and pre-eruption P-T-fO2-fH2O conditions of the dacite magma.

Scaillet, B. and MacDonald, R. (2001) Phase relations of peralkaline silicic magmas and petrogenetric implications. Journal of Petrology, vol 42, pp 825-845.

Scaillet, B. and MacDonald, R. (2003) Experimental constraints on the relationships between peralkaline rhyolites of the Kenya Rift Valley. Journal of Petrology, vol 44, pp 1867-1894.

Scaillet, B., Pichavant, M. and Roux, J. (1995) Experimental crystallization of leucogranite magmas. Journal of Petrology, vol 36, pp 663-705.

Schafer, B. Frischknecht, R., Gunther, D. and Dingwell, D.B. (1999) Determination of trace-element partitioning between fluid and melt using LA-ICP-MS analysis of synthetic fluid inclusions in glass. European Journal of Mineralogy, vol 11, pp 415-426.

Schenk, P.E. (1995a) Meguma Zone. In Geology of the Appalachian– Caledonian Orogen in Canada and Greenland. Edited by H. Williams. Geological Survey of Canada, Geology of Canada, No. 6, Chapt. 3, pp. 261–277. (Also Geological Society of America, The Geology of North America, Vol. F-1.)

Schenk, P.E. (1995b) Annapolis Belt. In Geology of the Appalachian– Caledonian Orogen in Canada and Greenland. Edited by H. Williams. Geological Survey of Canada, Geology of Canada, No. 6, Chapt. 4, pp. 367–383. (Also Geological Society of America, The Geology of North America, Vol. F-1.)

Schmidt, C., Romer, R.L., Wohlgemuth-Ueberwasser, C.C., Appelt, O. (2020) Partitioning of Sn and W between granitic melt and aqueous fluid. Ore Geology Reviews vol 117, 103263.

Shabani, A.A.T., Lalonde, A.E., and Whalen, J.B. (2003) Composition of biotite from granitic rocks of the Canadian Appalachian Orogen: A potential tectonomagmatic indicator? Canadian Mineralogist, vol 41, pp 1381-1396.

Shannon, R.D. (1976) Revised effective ionic radii and systematic studies of interatomic distances in halides and chaleogenides. Acta Crystallographica, A32, pp 751-767.

Shellnutt, J.G. and Dostal, J. (2012) An evaluation of crustal assimilation within the Late Devonian South Mountain Batholith, SW Nova Scotia. Geological Magazine, vol 149, pp 353–65.

Shellnutt, J.G. and Dostal, J. (2015) Granodiorites of the South Mountain Batholith (Nova Scotia, Canada) derived by partial melting of Avalonia granulite rocks beneath the Meguma terrane: implications for the heat source of the Late Devonian granites of the Northern Appalachians. Tectonophysics, vol 655, pp 206–212.

Shellnutt, G. and Dostal, J. (2019) Derivation of the Early Carboniferous Wedgeport pluton by crystal fractionation of a mafic parental magma: a rare case of an A-type granite within the Meguma terrane (Nova Scotia, Canada). Geological Magazine, vol 157, pp 248-262.

Shinohara, H., Iiyama, J.T. and Matsuo, S. (1989) Partition of chlorine compounds between silicate melt and hydrothermal solutions. Geochimica et Cosmochimica Acta, vol 53, pp 2617–2630.

Sisson, T.W. and Grove, T.L. (1993) Experimental investigations of the role of H_2O in calc-alkaline differentiation and subduction zone magmatism. Contributions to Mineralogy and Petrology, vol 113, pp.143-166.

Signorelli, S. and Carroll, M.R., (2000) Solubility and fluid–melt partitioning of Cl in hydrous phonolitic melts. Geochimica et Cosmochimica Acta, vol 64, pp 2851–2862.

Smythe, D. and Brenan, J.M. (2016) Magmatic oxygen fugacity estimated using zircon-melt partitioning of cerium. Earth and Planetary Science Letters, vol 453, pp 260-266.

Stone, M., Exley, C.S., and George, M.C. (1988) Composition of trioctahedral micas in the Cornubian batholith. Mineralogical Magazine, v. 52, p 175-192.

Stone, M. (2000) Petrogenetic implications from biotite compositional variations in the Cornubian granite batholith. Mineralogical Magazine, v. 64(4), p 729-735.

Stormer, J.C. and Carmichael, I.S.E. (1971) Fluorine-hydroxyl exchange in apatite and biotite: A potential igneous geothermometer. Contributions to Mineralogy and Petrology, v. 31, p 121-131.

Tate, M.C. and Clarke, D.B. (1995) Petrogenesis and regional tectonic significance of Late Devonian mafic intrusions in the Meguma Zone, Nova Scotia. Canadian Journal of Earth Sciences, vol 32, pp 1883–1898.

Tate, M.C. and Clarke, D.B. (1997) Compositional diversity among Late Devonian peraluminous granitoid intrusions in the Meguma Zone of Nova Scotia, Canada. Lithos, vol 39, pp 179–194.

Tattiche, B.C. and Blundy, J.D. (2017) Cu-Mo partitioning between felsic melts and saline-aqueous fluids as a function of X_{NaCleq}, fO_2, and fS_2. American Mineralogist, vol 102, pp 1987–2006.

Taylor, J.R. and Wall, V.J. (1993) Cassiterite solubility, tin speciation, and transport in a magmatic aqueous phase. Economic Geology, vol 88, pp 437-460.

Tischendorf, G., Forster, H.-J., and Gottesmann, B. (2001) Minor- and trace-element composition of trioctahedral micas: a review. Mineralogical Magazine, vol 65, pp. 249–276.

Toplis, M.J. and Carroll, M.R. (1995) An experimental study of the influence of oxygen fugacity on Fe-Ti oxide stability, phase relations, and mineral-melt equilibria in ferro-basaltic systems. Journal of Petrology, vol 36, pp. 1137-1170.

Uchida, E., Sakamori, T. and Matsunaga, J. (2002) Aqueous speciation of lead and tin chlorides in supercritical hydrothermal solutions. Geochemical Journal, vol. 36, pp. 61-72.

Uchida, E., Endo, S. and Makino, M. (2007) Relationship between solidification depth of granitic rocks and formation of hydrothermal ore deposits. Resource Geology, vol 57, pp 47-56.

Volfinger M., Robert, J.L., Vielzeuf, D., and Neiva, A.M.R. (1985) Structural control of the chlorine content of OH-bearing silicates (micas and amphiboles). Geochimica et Cosmochimica Acta, v. 49, pp. 37-48.

Wallace, G.M.B (1988) Petrogenesis of the McGerrigle Plutonic Complex: Mineralogical and oxygen isotopic constraints. Unpublished M.Sc. thesis, McGill University, 330 p.

Waldron, J.W.F. (1992) The Goldenville–Halifax transition, Mahone Bay, Nova Scotia: relative sea-level rise in the Meguma source terrane. Canadian Journal of Earth Sciences, vol 29, pp 1091–1105.

Whalen, J. B. and Chappell, B. W. (1988) Opaque mineralogy and mafic mineral chemistry of I- and S-type granites of the Lachlan fold belt, Southeast Australia. American Mineralogist, vol 73, pp 281–296.

Webster, J.D. (1990) Partitioning of F between H2O and CO2 fluids and a topaz rhyolite melt. Implications for mineralizing magmatic-hydrothermal fluids in F-rich granitic systems. Contributions to Mineralogy and Petrology 104, 424–438.

Webster, J.D. and De Vivo, B. (2002) Experimental and modeled solubilities of chlorine in aluminosilicate melts, consequences of magma evolution, and implications for exsolution of hydrous chloride melt at Mt. Somma-Vesuvius. American Mineralogist, v. 87, p. 1046-1061.

Webster, J.D. and Holloway, J.R. (1988) Experimental constraints on the partitioning of Cl between topaz rhyolite melt and H_2O and H_2O+CO_2 fluids: new implications for granitic differentiation and ore deposition. Geochimica et Cosmochimica Acta 52, 2091–2105.

Webster, J.D. and Holloway, J.R. (1990) Partitioning of F and Cl between magmatic hydrothermal fluids and highly evolved granitic magmas. Geological Society of America Special Papers vol 246, pp 21–34.

Webster, J.D., Goldoff, B.A., Flesch, R.N., Nadeau, P.A., and Silbert, Z.W. (2017) Hydroxyl, Cl, and F partitioning between high-silica rhyolitic melts-apatite-fluid(s) at 50-200 MPa and 700-1000 degrees C. American Mineralogist, vol 102, pp 61-74.

Webster, J.D., Baker, D.R., and Aiuppa, A. (2018) Halogens in mafic and intermediate-silicate content magmas: In (Harlov, D.E., and Aranovich, L.) The Role of Halogens in Terrestrial and Extraterrestrial Geochemical Processes. Springer. p. 307-430.

Williams, H. (1979) The Appalachian Orogen in Canada. Canadian Journal of Earth Sciences, 16: 792–807.

Williams-Jones, A.E. and Heinrich, C.A. (2005) Vapor transport of metals and the formation of magmatic-hydrothermal ore deposits. Economic Geology vol 100, pp 1287–1312.

Wones, D. and Eugster, H.P (1965) The stability of biotite: Experiment, theory and application. American Journal of Science, vol 30, pp 1228-1272.

Yang, X.-M. and Lentz, D.R. (2005) Chemical composition of rock-forming minerals in gold-related granitoid intrusions, southwestern New Brunswick, Canada: implications for crystallization conditions, volatile exsolution, and fluorine-chlorine activity. Contributions to Mineralogy and Petrology, 150: 287–305.

Zajacz, Z., Halter, W. E., Pettke, T., and Guillong, M. (2008) Determination of fluid/melt partition coefficients by LA-ICPMS analysis of co-existing fluid and silicate melt inclusions: Controls on element partitioning: Geochimica et Cosmochimica Acta, v. 72, p. 2169–2197.

Zhang C., Holtz F., Ma C., Wolff P. and Li X. (2012) Tracing the evolution and distribution of F and Cl in plutonic systems from volatile-bearing minerals: a case study from the Liujiawa pluton (Dabie orogen, China). Contributions to Mineralogy and Petrology, vol 164, pp 859–879.

Zhang, X., Xu, X., Xia, Y., and Zhao, K. (2021) Crystallization and melt extraction of a garnet-bearing charnockite from South China: constraints from petrography, geochemistry, mineral thermometry, and rhyolite-MELTS modelling. American Mineralogist, vol 106, pp 461-480.

Zhang, C., Li, X., Behrens, H. and Holtz, F. (2022) Partitioning of OH-F-Cl between biotite and silicate melt: Experiments and an empirical model. Geochimica et Cosmochimica Acta, vol 317, pp 155–179.

Zhao, D., Essene, E.J., and Zhang, Y. (1999) An oxygen barometer for rutile–ilmenite assemblages: oxidation state of metasomatic agents in the mantle. Earth and Planetary Science Letters, vol 166, p. 127–137.

Zhao, P., Zajacz, Z., Tsay, A., and Yuan, S. (2022) Magmatic-hydrothermal tin deposits form in response to efficient tin extraction upon magma degassing. Geochimica et Cosmochimica Acta vol 316, p. 331–346

Zhu C. and Sverjensky D. A. (1991) Partitioning of F–Cl–OH between minerals and hydrothermal fluids. Geochimica et Cosmochimica Acta 55, p. 1837–1858.

This is the peer-reviewed, final accepted version for American Mineralogist, published by the Mineralogical Society of America.
The published version is subject to change. Cite as Authors (Year) Title. American Mineralogist, in press.
DOI: https://doi.org/10.2138/am-2022-8691. http://www.minsocam.org/

1134 # List of Tables

Table 1: Summary of Samples

Sample	Texture	Easting	Northing	Lithology	Pluton	Phase	Grain Size	Modal % Biotite	Degree of Chloritization	Frequency of Inclusions In Biotite
18JC-0001	Porphyritic K-Feldspar	449381	4938638	MBMG	HP	2	CG	7	0	2
18JC-0003	Porphyritic K-Feldspar	449154	4933734	MBMG	HP	2	MG	5	1	3
18JC-0004	Porphyritic K-Feldspar + Plagioclase	449507	4927713	MBMG	HP	2	FG	2	1	4
18JC-0008	Equigranular	447604	4943099	BGD	HP	2	CG	10	0	3
18JC-0010	Equigranular (Excluding Biotite)	422977	4948571	FGLMG	NRP	2	CG	5	0	3
18JC-0012	Porphyritic K-Feldspar	428976	4951313	BMG	SL	1	MG	5	0	2
18JC-0016	Equigranular	425491	4949579	FGLMG	NRP	2	MG	1	3	1
18JC-0021	Porphyritic K-Feldspar + Plagioclase	399559	4968101	BGD	STP	1	CG	10	0	3
19BM-0001	Equigranular (Excluding Biotite)	353830	4943146	BMG	LRP	1	CG	10	0	2
19BM-0002	Equigranular (Excluding Biotite)	352144	4943011	FGLMG	EDP	2	CG	3	0	1
19BM-0004	Equigranular	348166	4948721	BGD	SGP	1	MG	15	0	2
19BM-0006	Porphyritic K-Feldspar	342272	4953756	BMG	SGP	1	CG	5	1	3
19BM-0008	Equigranular (Excluding Biotite)	337383	4967261	BMG	CLP	1	MG to CG	3	0	1
19BM-0015	Porphyritic K-Feldspar	294378	4882723	CGLMG	DLP	2	CG	3	3	1
19BM-0017	Porphyritic K-Feldspar , Sheared	277040	4879188	CGLMG	DLP	2	CG	1	0	4
A03-3000	Porphyritic K-Feldspar	302302	4892405	CGLMG	DLP	2	CG	10	0	2
A03-3007	Equigranular (Excluding Biotite)	310603	4899025	CGLMG	DLP	2	CG	5	1	2
A03-3024	Equigranular (Excluding Biotite)	304424	4902233	CGLMG	DLP	2	CG	3	1	3
A04-3000	Equigranular (Excluding Biotite)	291311	4902100	CGLMG	DLP	2	CG	3	0	3
A05-0039	Porphyritic K-Feldspar	288010	4907016	CGLMG	DLP	2	CG	1	2	4
A06-3015	Equigranular	317448	4928202	BMG	SGP	1	MG to CG	7	0	2
A06-3017	Equigranular (Excluding Biotite)	304836	4926287	BMG	SGP	1	CG	5	2	3
A09-2224	Equigranular (Excluding Biotite)	409491	4952558	FGLMG	NRP	2	MG to CG	3	0	3
A09-2378	Equigranular (Excluding Biotite)	397167	4948103	CGLMG	NRP	2	CG	3	1	3
A10-3014	Equigranular	375014	4949375	BMG	STP	1	MG to CG	7	1	1
A10-3020	Equigranular	378162	4937604	CGLMG	NRP	2	CG	2	1	2
A10-3056	Equigranular	361726	4954282	FGLMG	EDP	2	FG	1	0	1
A10-3086	Equigranular	351505	4955630	BGD	SGP	1	CG	12	0	2
A10-3100	Porphyritic K-Feldspar	350002	4947283	CGLMG	EDP	2	MG	5	0	1
A11-2239	Equigranular	328128	4953209	CGLMG	WDP	2	MG	2	0	2
A11-2286	Equigranular	322566	4946971	BMG	SGP	1	FG	15	0	1
A11-3002	Porphyritic K-Feldspar	311183	4957463	BGD	SGP	1	MG	7	0	2
A11-3013	Equigranular	320968	4953585	CGLMG	WDP	2	CG	3	0	3
A14-0007	Porphyritic K-Feldspar	340054	4958821	CGLMG	WDP	2	CG	3	3	2
A14-1032	Equigranular	323073	4966877	BMG	SGP	1	CG	5	0	3
A15-0044-2	Equigranular	367018	4956918	FGLMG	EDP	2	MG	1	0	2
A15-0057	Equigranular	373457	4970241	BMG	STP	1	FG to MG	15	1	2
A16-1171	Equigranular	405875	4964951	CGLMG	NRP	2	MG	1	1	1
A16-1172	Equigranular (Excluding Biotite)	409658	4964993	BGD	FIP	1	CG	5	1	3
A16-1174	Porphyritic K-Feldspar	408258	4961032	CGLMG	NRP	2	MG	3	1	2
A16-1256	Equigranular	392565	4960613	MLG	NRP	2	MG to CG	5	0	2
A16-1281	Equigranular	401547	4971585	BGD	STP	1	CG	7	0	3
A16-3052	Equigranular	417648	4968153	BGD	FIP	1	CG	10	1	4
D12-0033	Porphyritic K-Feldspar	443438	4935686	MBMG	HP	2	MG to CG	5	1	3
D12-0045-C	Equigranular (Excluding Biotite)	439114	4932685	MBMG	HP	2	MG to FG	7	2	2
D12-0050	Porphyritic K-Feldspar	425746	4930048	CGLMG	HP	2	Mg	5	2	3
D12-0103-2	Equigranular (Excluding Biotite)	442747	4942774	CGLMG	HP	2	CG to MG	7	3	1
D12-3082	Equigranular	431593	4929963	CGLMG	HP	2	CG	3	1	1
D13-2004	Equigranular (Excluding Biotite)	433703	4964115	BGD	FIP	1	CG	10	1	2

BGD= Biotite Granodiorite; BMG= Biotite Monzogranite; MBMG= Muscovite Biotite Monzogranite; CGLMG= Coarse-grained Leucomonzogranite; FGLMG= Fine-grained Leucomonzogranite; MLG= Muscovite Leucogranite
CLP= Cloud Lake Pluton; DLP= Davis Lake Pluton; EDP= East Dalhousie Pluton; FIP= Five Mile Lake Pluton; HP= Halifax Pluton; LRP= Little Round Lake Pluton;
NRP= New Ross Pluton; SGP= Scragg Lake Pluton; SLP= Sandy Lake Pluton; STP= Salmon Tail Pluton; WDP= West Dalhousie Pluton

Degree of Chloritization
0) Negligible: No alteration to one or two grains with minor alteration on grain boundaries
1) Minor alteration: Most grains have alteration on grain boundaries or a few grains have been completely replaced by chlorite
2) Significant alteration: Almost all grains have alteration with multiple grain being completely altered. Less then half of the Biotite grains have ben altered to chlorite
3) Widespread alteration: Almost no Biotite remains

Frequency of Inclusions
1) Rare: One or two grains have inclusions
2) Uncommon: Less then 2/3 the grains have inclusions
3) Common: Almost all grains have them or a few grains have multiple of inclusions
4) Abundant : All grain have multiple inclusions

CG: Coarse grained (>2 mm)
MG: Medium grained (1-2mm)
FG: Fine Grained (<1 mm)

Coordinates are in UTM 20 NAD 83

1135

1136

1137

This is the peer-reviewed, final accepted version for American Mineralogist, published by the Mineralogical Society of America.
The published version is subject to change. Cite as Authors (Year) Title. American Mineralogist, in press.
DOI: https://doi.org/10.2138/am-2022-8691. http://www.minsocam.org/

Table 2. Summary of parameters for halogen crystallization model

species	Initial melt concentration (C_o)	notes	$D_{mineral/melt}$ or $D_{vapour/melt}$	reference
fluorine	600 μg/g	consistent with biotite data; whole-rock F-SiO_2 relations	$D_{apatite/melt}$ = 3 $D_{biotite/melt}$ = 2 $D_{vapour/melt}$ = 0.3	Mathez and Webster (2005); Icenhower and London (1997); Webster and Holloway (1990)
chlorine	27 (undersat), 60 (sat) μg/g	consistent with biotite data	$D_{apatite/melt}$ = 1 $D_{biotite/melt}$ = 5 $D_{vapour/melt}$ = 17	Mathez and Webster (2005); Icenhower and London (1997); Signorelli and Carroll (2000); Webster and Holloway (1989)
titanium	0.11 wt%	Estimated from biotite/melt partitioning	D_{bulk} = 1.5, consistent with 2% biotite (D=24) and 1% ilmenite+/-rutile (D>100)	Icenhower and London (1995)
H_2O	7.0 wt%	comparison to 300 MPa water-saturated liquidus	Fixed at 300 MPa solubility	Holz et al. (2001)

1138

This is the peer-reviewed, final accepted version for American Mineralogist, published by the Mineralogical Society of America.
The published version is subject to change. Cite as Authors (Year) Title. American Mineralogist, in press.
DOI: https://doi.org/10.2138/am-2022-8691. http://www.minsocam.org/

List of Figures

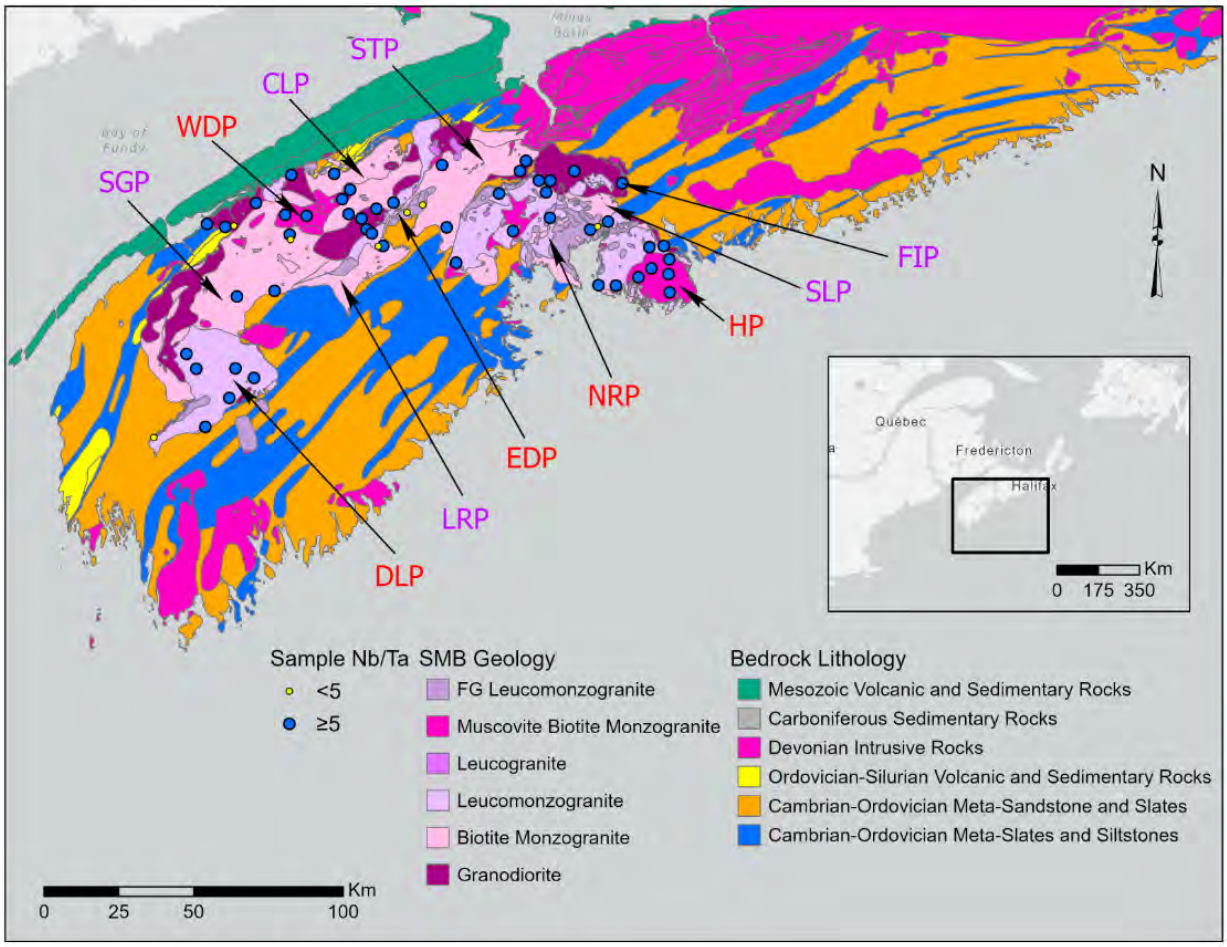

Figure 1. Map of the Meguma Lithotectonic zone in southwestern mainland Nova Scotia, Canada showing the distribution of major stage 1 (purple text) and stage 2 (red text) plutons of the South Mountain Batholith and the samples chosen for this study. Pluton boundaries and sample geochemical data from MacDonald (2001) and references therein. SMB geology overlay modified from Fisher (2006). Pluton abbreviations and phase are as follows: Davis Lake Pluton (DLP; 2); Little Round Lake Pluton (LRP; 1); East Dalhousie Pluton (EDP; 2); New Ross Pluton (NRP; 2); Halifax Pluton (HP; 2); Sandy Lake Pluton (SLP; 1); Five Mile Lake Pluton (FIP; 1); Salmon Tail Pluton (STP; 1); Cloud Lake Pluton (CLP; 1); West Dalhousie Pluton (WDP; 2); Scrag Lake Pluton (SGP; 1).

This is the peer-reviewed, final accepted version for American Mineralogist, published by the Mineralogical Society of America.
The published version is subject to change. Cite as Authors (Year) Title. American Mineralogist, in press.
DOI: https://doi.org/10.2138/am-2022-8691. http://www.minsocam.org/

1150

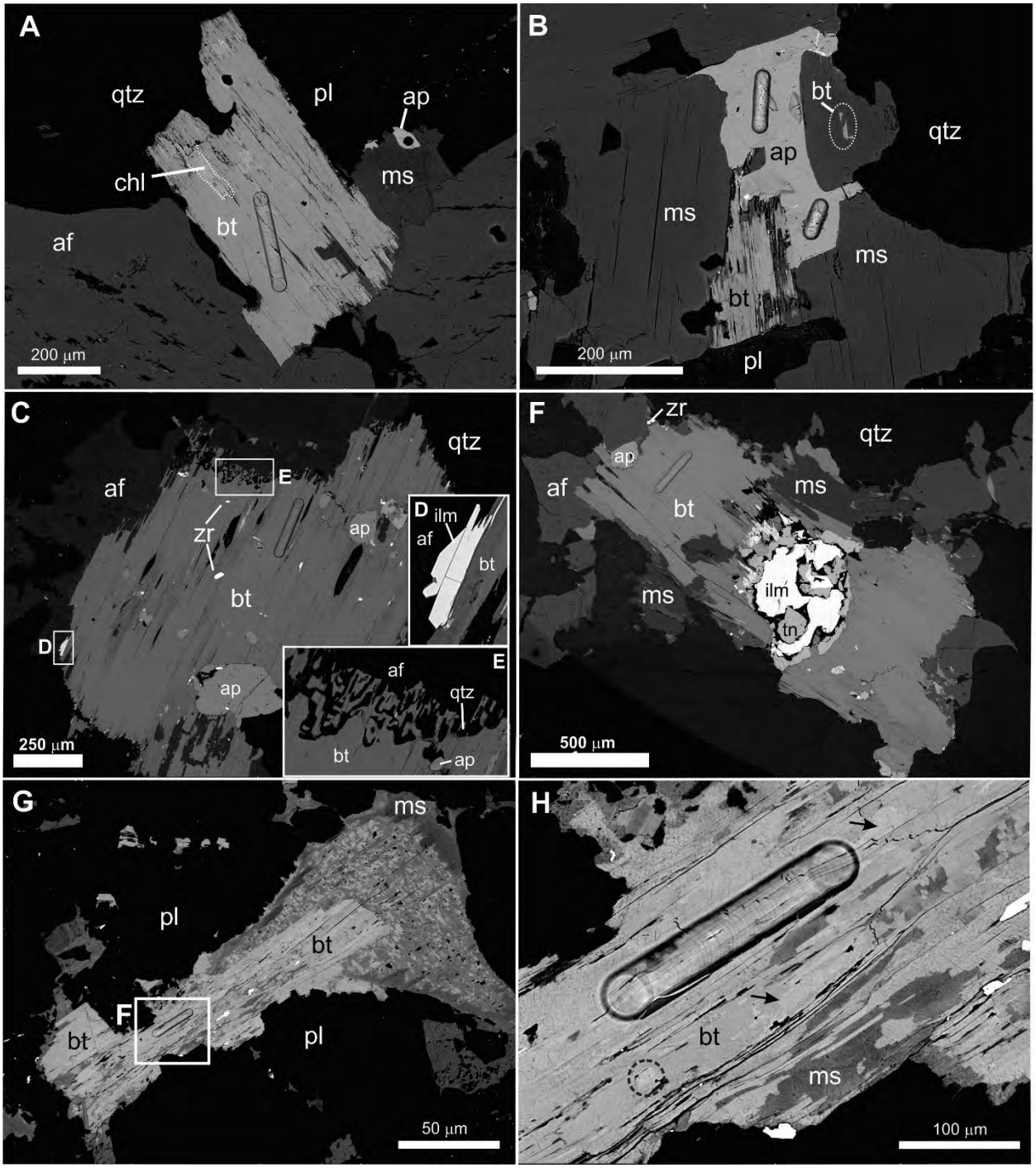

1151

1152

1153

1154

1155

Figure 2 (preceding page). Images from samples A09-2224 (A-F) and A16-1256 (G-H; both New Ross Pluton) showing representative mineralogical association and textural characteristics of biotite and apatite in phase 2 plutons of the SMB. Mineralogical associations and textural characteristics of biotite and apatite in stage 2 plutons of the SMB. Images are from back-scattered electron (BSE) scanning electron microscopy (SEM). Mineral abbreviations: bt=biotite; pl=plagioclase; chl=chlorite; qtz=quartz; ap=apatite; af=alkali feldspar; ms=muscovite; mz=monazite; zr=zircon; ilm=ilmenite; tn=titanite. (A) Bt is interstitial to pl, qtz, af, and primary ms, and is coeval with ap. Partial replacement of bt by chl is visible (white dashed outline). A channel excavated during a laser ablation traverse in bt is visible in the center of the grain, and a circular laser ablation pit is visible in the ap grain. (B) Coarse-grained ms encloses interstitial bt-ap. Remnants of bt replaced by ms are circled in dashed oval. The central bt grain is heavily chloritized. (C) Bt interstitial to qtz and af, showing abundant accessory minerals including in, and along the margins of, the bt grain (e.g., ap, zr, ilm). Inset (D) shows magnified view of ilmenite along the af-bt grain contact. Inset (E) shows the contact of the bt with the surrounding qtz/af as containing a symplectic intergrowth of af, bt, and qtz. (F) Bt-af intergrowth showing partial replacement of bt by ms, accessory ap and zr. The bt appears to have grown over a "core" of ilm-tn. (G) Interstitial bt surrounded in pl. The bt is surrounded in an epitaxial overgrowth of a mica with a mottled appearance (cf. "IMP - intermediate mica phase"; Clarke and Bogutyn, 2003) and ms at its outermost edge in the sequence biotite→IMP→muscovite. (H) Magnified view of the area in the white box in (G) showing a laser ablation channel in fresh bt and compositional variation (gray-scale variations) in the bt (biotite→IMP). The lightest gray-scale patches (e.g., black dashed circle; black arrow) are the most Fe-rich, and freshest domains of the original bt, whereas darker grey domains throughout most of the grain have lower Fe content.

This is the peer-reviewed, final accepted version for American Mineralogist, published by the Mineralogical Society of America.
The published version is subject to change. Cite as Authors (Year) Title. American Mineralogist, in press.
DOI: https://doi.org/10.2138/am-2022-8691. http://www.minsocam.org/

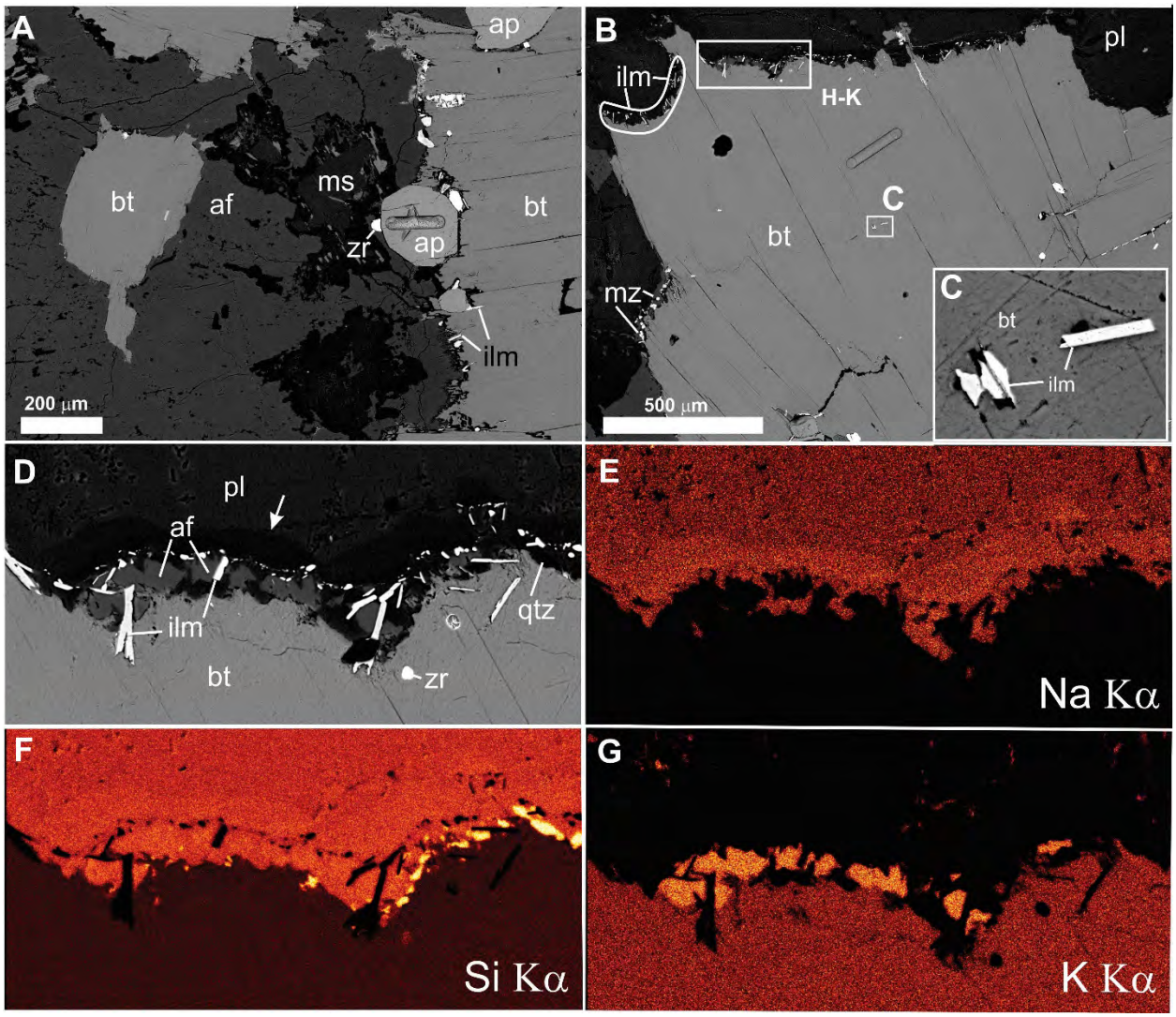

Figure 3. Images from sample A15-0057 (Salmon Tail Pluton) showing representative mineralogical association and textural characteristics of biotite and apatite in phase 1 plutons of the SMB. Mineral abbreviations same as in Figure 1. SEM-BSE images and X-ray EDS maps. (A) Bt-af intergrowths showing a large accessory ap grain along the bt-af interface (containing a laser ablation channel). Accessory ilm is also abundant along this interface. Late ms alteration is also seen within the af. (B) Interstitial bt surrounded in pl. Accessory ilm is abundant along the bt grain margin as partial and complete inclusions, but also as complete inclusions deeper in the bt grain (magnified view inset C). Grains of mz occur along the biotite grain margin, included in af. (C) Magnified view of inset in (B) showing the contact between pl and bt containing intergrowths of af, qtz, and ilm. Notably the pl is zoned in this contact region. (E-G) are EDS maps of X-ray intensities (E:Na K-alpha line; F:Si K-alpha line; G: K K-alpha line) along the bt contact with pl, showing the af-qtz-ilm assemblage and the zoning to more albitic pl nearest the contact.

This is the peer-reviewed, final accepted version for American Mineralogist, published by the Mineralogical Society of America.
The published version is subject to change. Cite as Authors (Year) Title. American Mineralogist, in press.
DOI: https://doi.org/10.2138/am-2022-8691. http://www.minsocam.org/

1193 A)

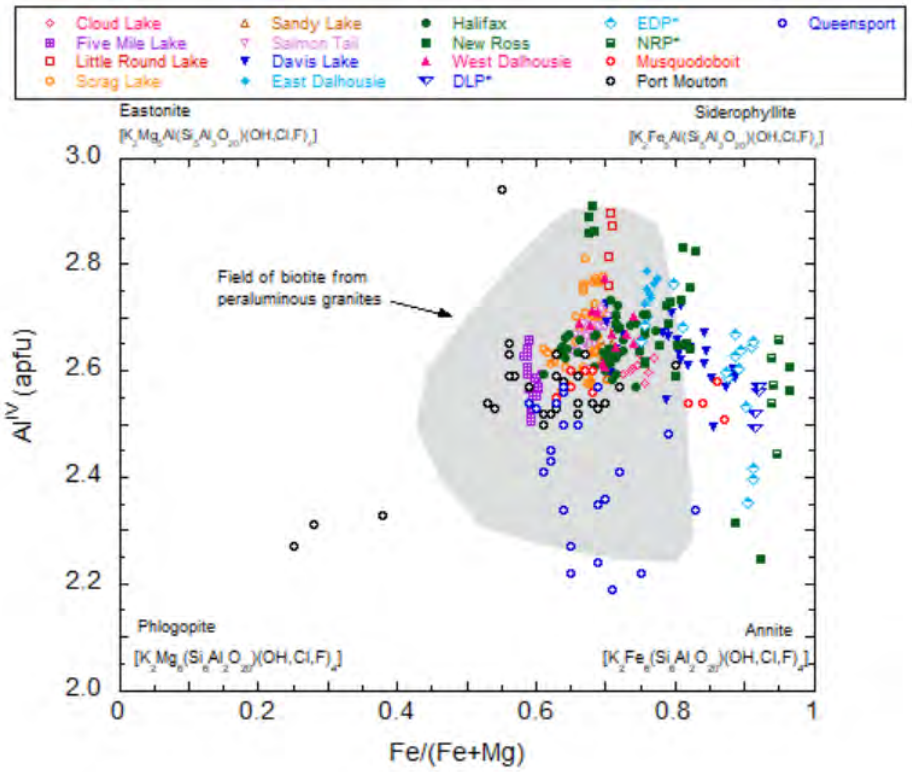

1194

1195 B)

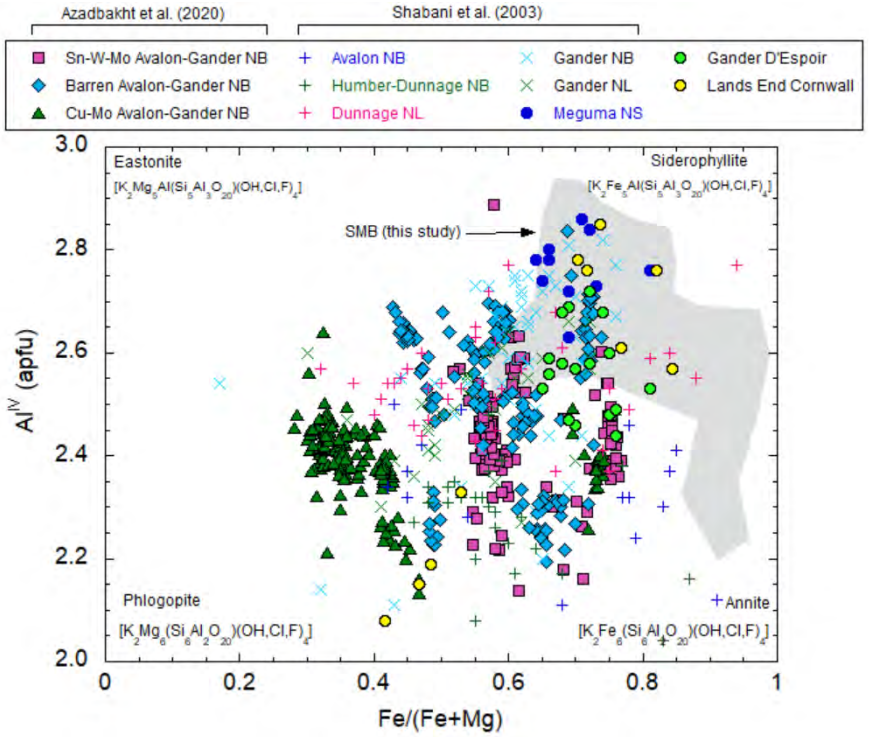

1196

Figure 4 (previous page). The proportion of tetrahedral aluminum (Al^{IV}) as a function of Fe/(Fe+Mg) in biotite from A) the SMB and other Meguma Tectonic zone felsic plutons and B) other northern Appalachian Devonian-aged felsic plutons as well as the peraluminous Land's End pluton, Cornwall. All values are calculated on the basis of 22 oxygen equivalents. Samples from the SMB are classified as Al-rich biotite, with a significant annite component. Here and elsewhere, symbols marked as DLP*, EDP* and NRP* are those samples with Nb/Ta < 5. The field of biotite from peraluminous granites in A) is from Clarke (1981). The SMB and the Musquodoboit plutons comprise the "Central Series", whereas the Port Mouton and Queensport pluton comprise the "Peripheral Series" of Tate and Clarke (1997). Data sources: Musquodoboit: MacDonald (1981); Port Mouton: Douma (1988); Queensport: Ham (1988); Barren and Cu-Mo or Sn-W-Mo-mineralized Avalon-Gander Tectonic zones: Azadbakht et al. (2020); Gander D'Espoir: Bennett (1990); Other northern Appalachian occurrences: Shabani et al. (2003); Lands End, Cornwall: Stone et al., (1988); Stone, (2000); Müller et al., (2006).

This is the peer-reviewed, final accepted version for American Mineralogist, published by the Mineralogical Society of America.
The published version is subject to change. Cite as Authors (Year) Title. American Mineralogist, in press.
DOI: https://doi.org/10.2138/am-2022-8691. http://www.minsocam.org/

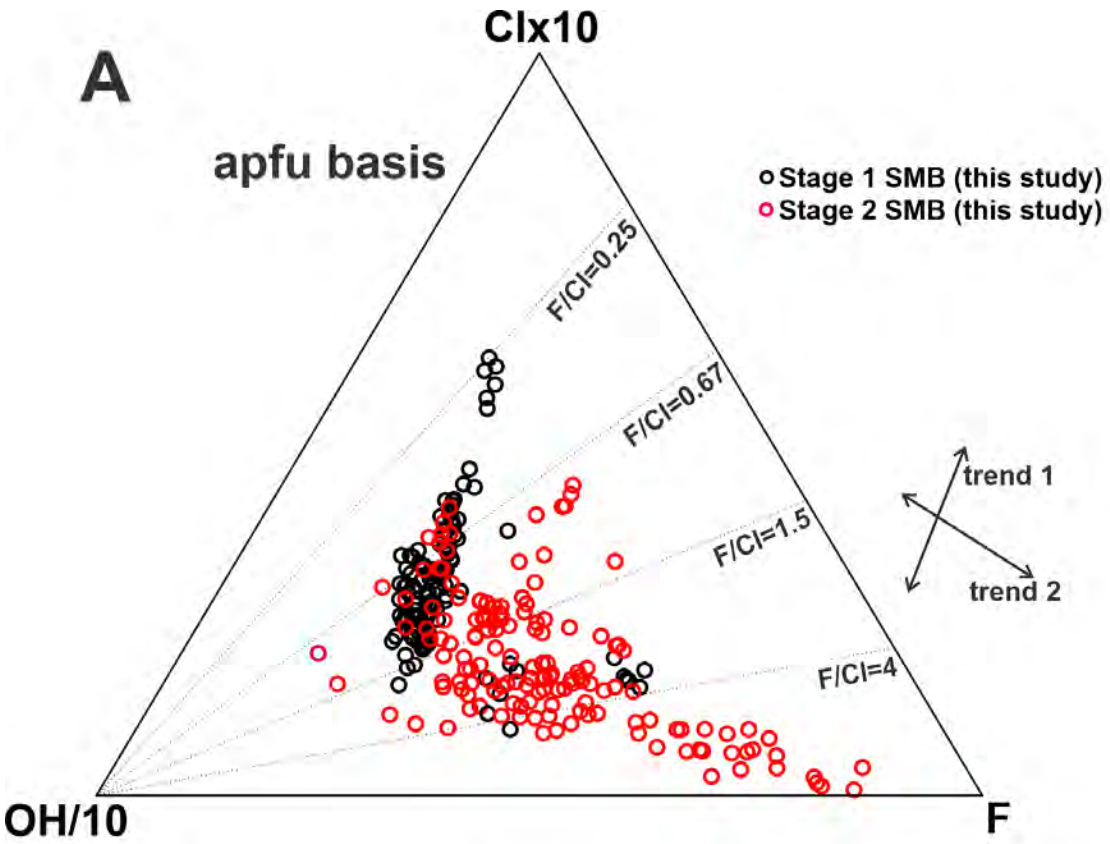

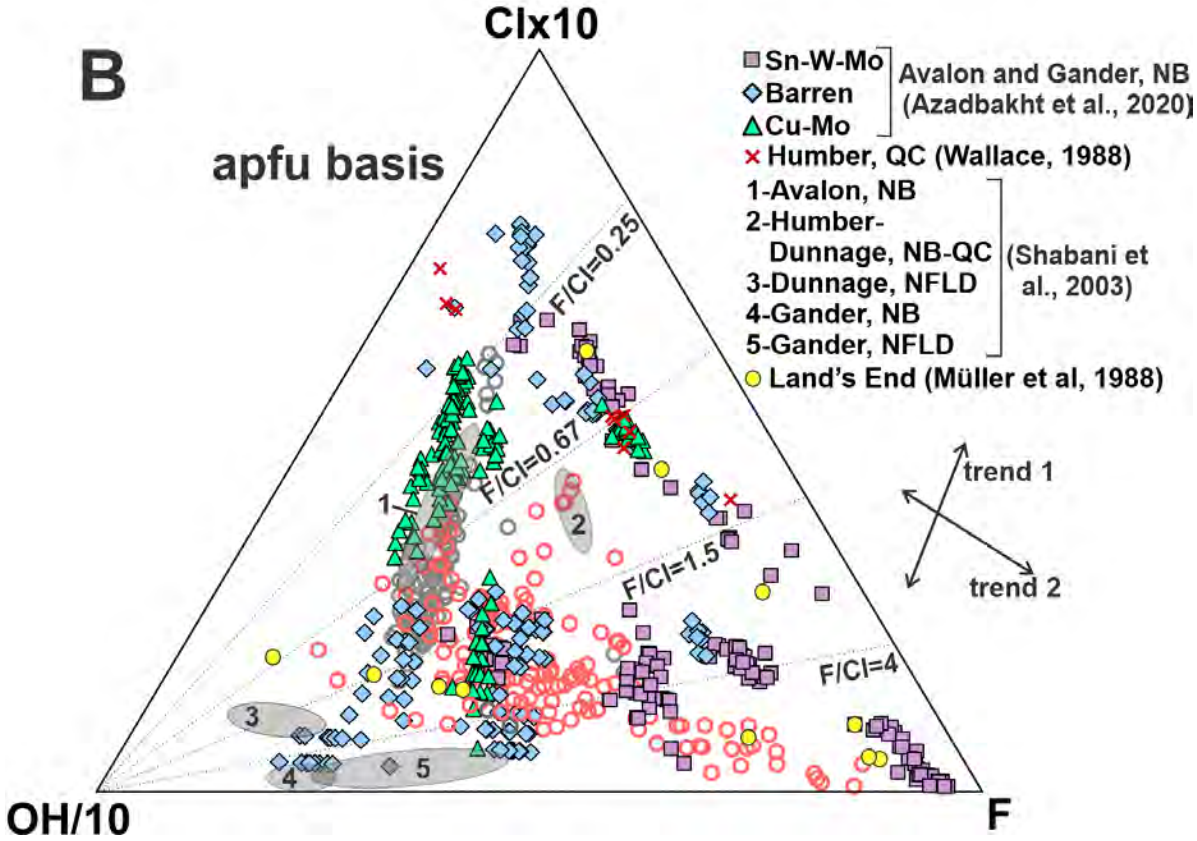

1209

Figure 5 (preceding page). Ternary diagram summarizing the variation in OH, F and Cl site occupancy in biotite from a) Stage 1 and Stage 2 plutons from the SMB, and b) other occurrences as per Figure 4. See the text for an explanation of trend 1 *vs.* trend 2.

This is the peer-reviewed, final accepted version for American Mineralogist, published by the Mineralogical Society of America.
The published version is subject to change. Cite as Authors (Year) Title. American Mineralogist, in press.
DOI: https://doi.org/10.2138/am-2022-8691. http://www.minsocam.org/

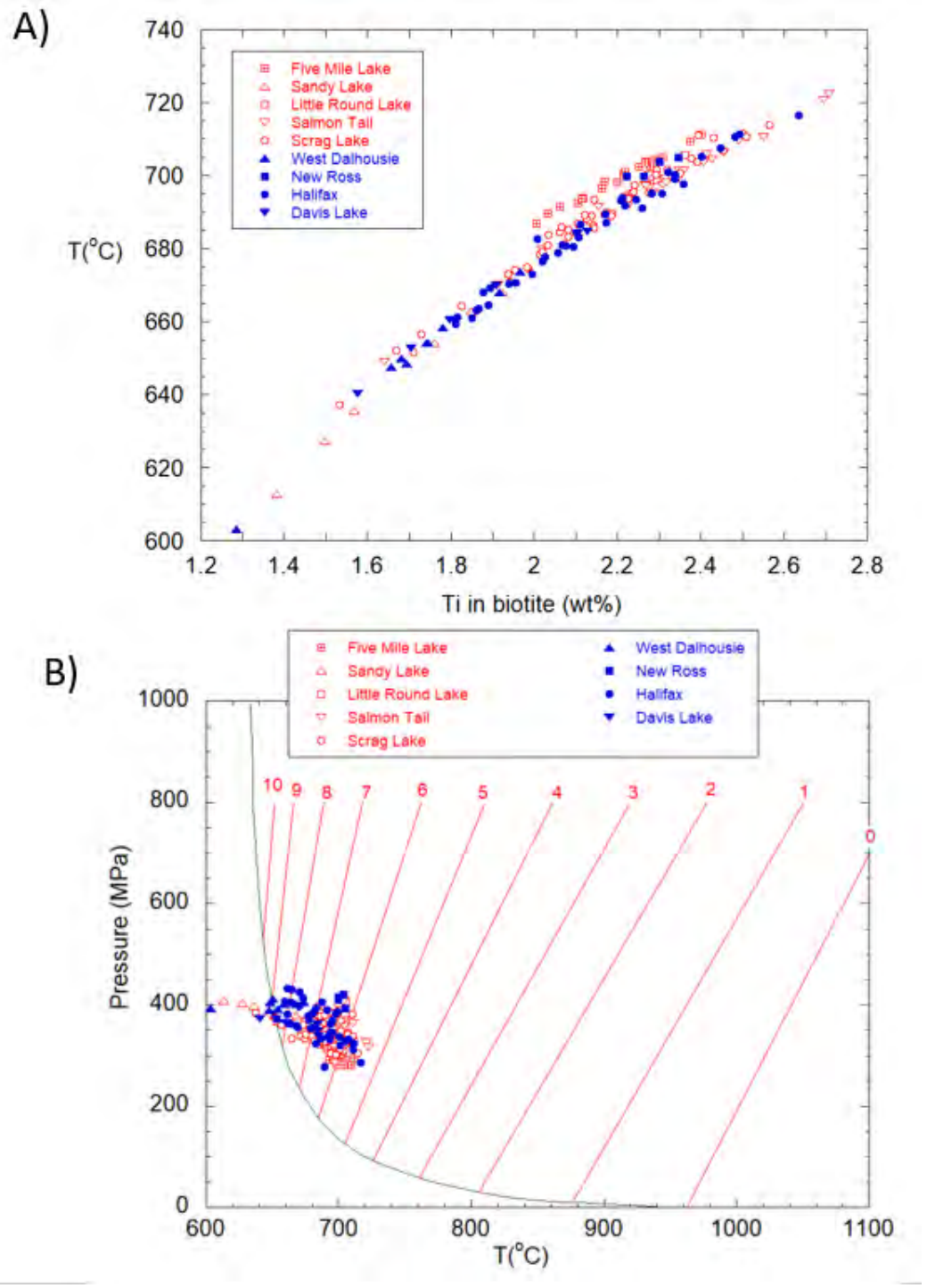

Figure 6. A) Temperatures of biotite formation calculated from the Ti-in-biotite geothermometer of Henry et al. (2005) as a function of the biotite Ti concentration. **B)** Pressure-temperature estimates of biotite formation using the Ti-in-biotite geothermometer of Henry et al. (2005) and the Al-in-biotite geobarometer of Uchida et al. (2007). P-T estimates are superimposed on the water-saturated liquidus curves (red) emanating from the water saturated solidus (green) for subaluminous compositions proposed by Holtz et al. (2001). The liquidus curves (labeled according to H_2O content) indicate the minimum water content that can be dissolved in melts at a given P and T.

This is the peer-reviewed, final accepted version for American Mineralogist, published by the Mineralogical Society of America.
The published version is subject to change. Cite as Authors (Year) Title. American Mineralogist, in press.
DOI: https://doi.org/10.2138/am-2022-8691. http://www.minsocam.org/

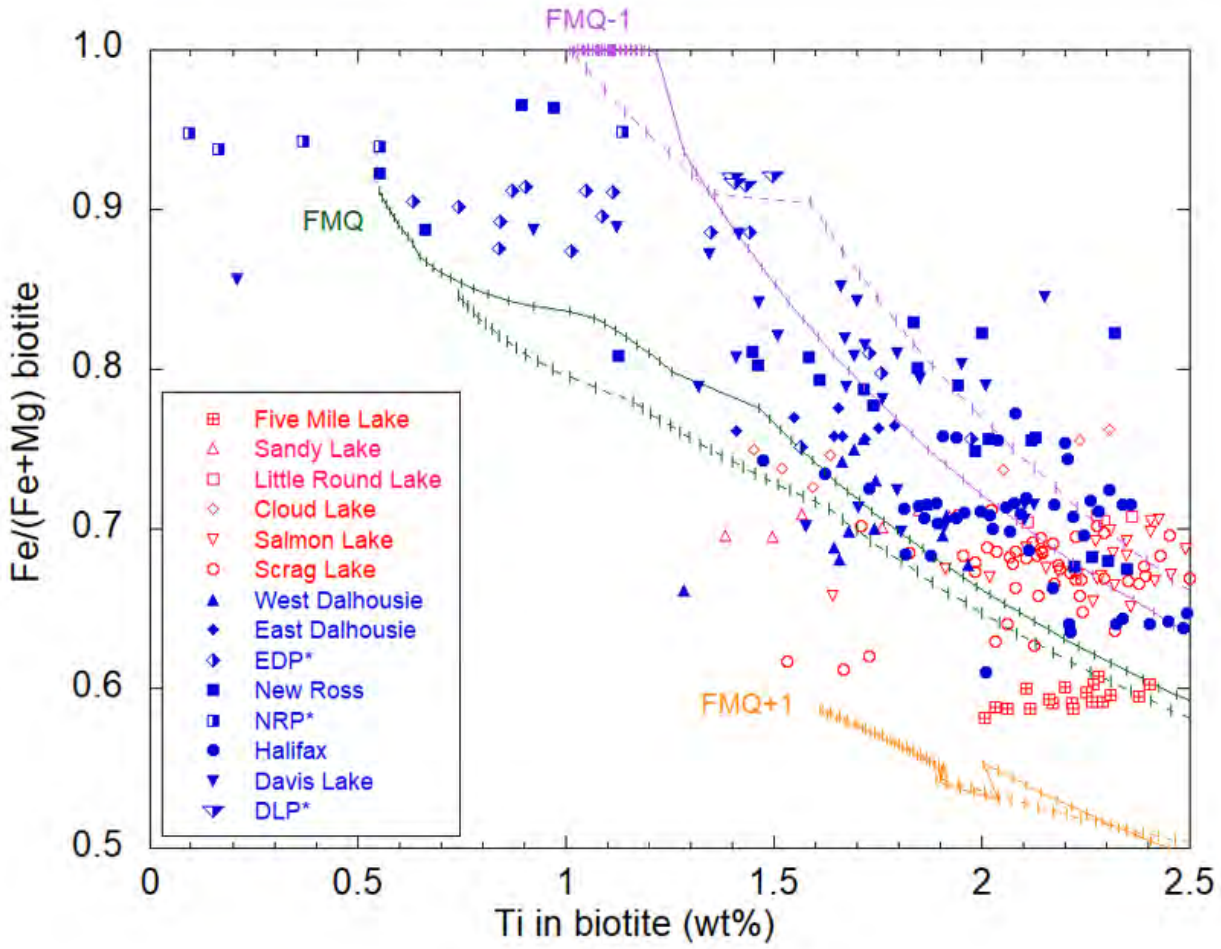

Figure 7. Variation in the biotite molar Fe/(Fe+Mg) (Fe#) as a function of Ti concentration (wt%) for samples from the SMB compared to calculated biotite compositions from the MELTS thermodynamic model. Model curves with vertical tick marks correspond to biotite produced in fractional crystallization models involving initial bulk compositions with molar Fe/Fe+Mg spanning the range of the most Ti-rich, silica-poor whole-rock compositions (0.5 and 0.65, dashed and solid curves, respectively) at oxygen fugacity of FMQ and FMQ+/- 1. Melt crystallization temperature, and liquid fraction, decreases right to left on this diagram, with all the MELTS simulation curves terminating at 662°C and a final melt fraction of 10%. Note the regular increase in Fe# with decreasing Ti content exhibited by the SMB data and captured by the model curves, indicating that the Fe#-Ti variation is a measure of falling temperature, and therefore magma evolution. The relatively high values of biotite Fe# at a given Ti content are best reproduced by crystallization models more reduced than FMQ. Samples marked with * have whole-rock Nb/Ta < 5.

This is the peer-reviewed, final accepted version for American Mineralogist, published by the Mineralogical Society of America.
The published version is subject to change. Cite as Authors (Year) Title. American Mineralogist, in press.
DOI: https://doi.org/10.2138/am-2022-8691. http://www.minsocam.org/

1237

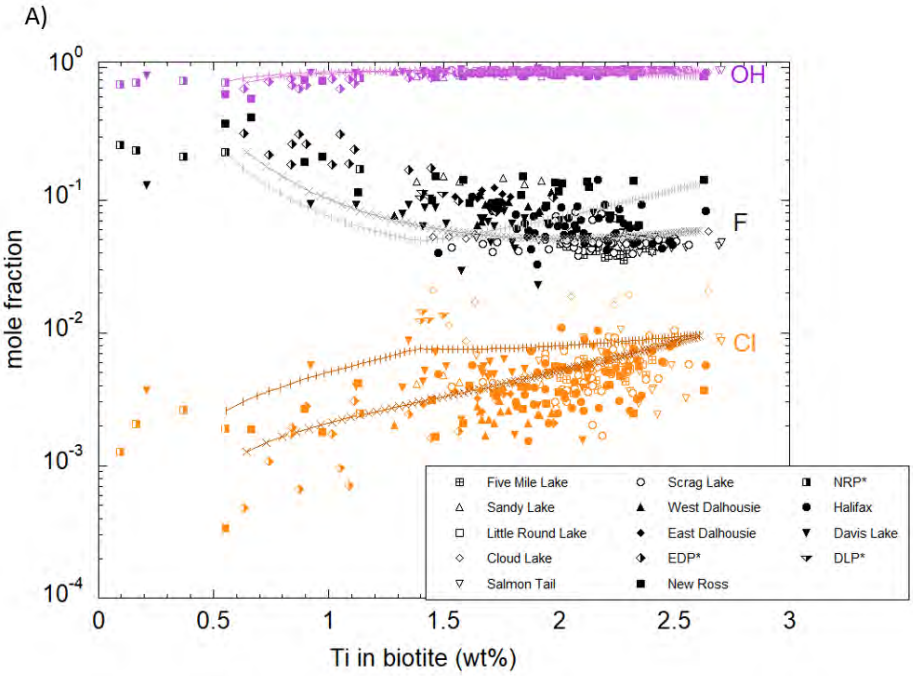

1238

1239

1240

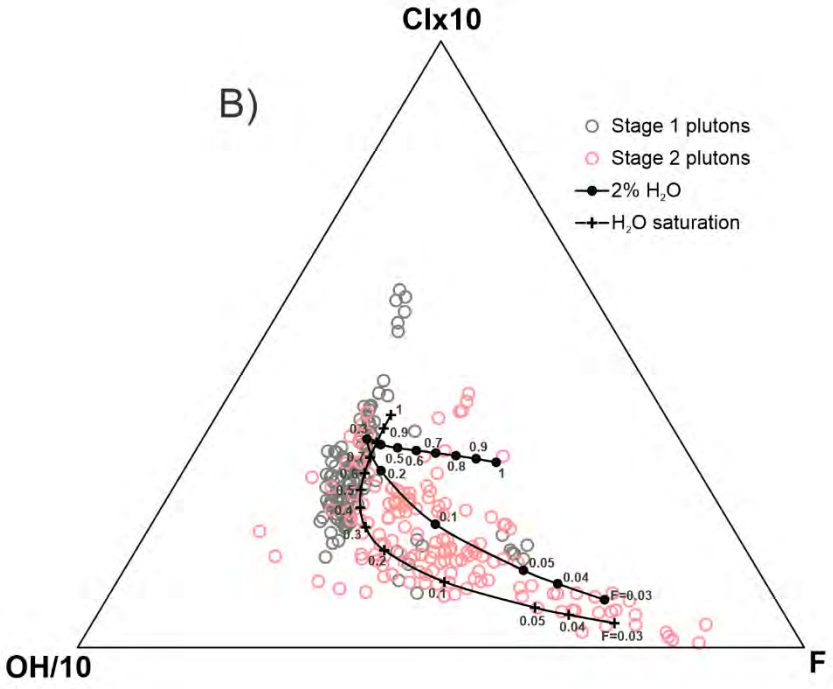

This is the peer-reviewed, final accepted version for American Mineralogist, published by the Mineralogical Society of America.
The published version is subject to change. Cite as Authors (Year) Title. American Mineralogist, in press.
DOI: https://doi.org/10.2138/am-2022-8691. http://www.minsocam.org/

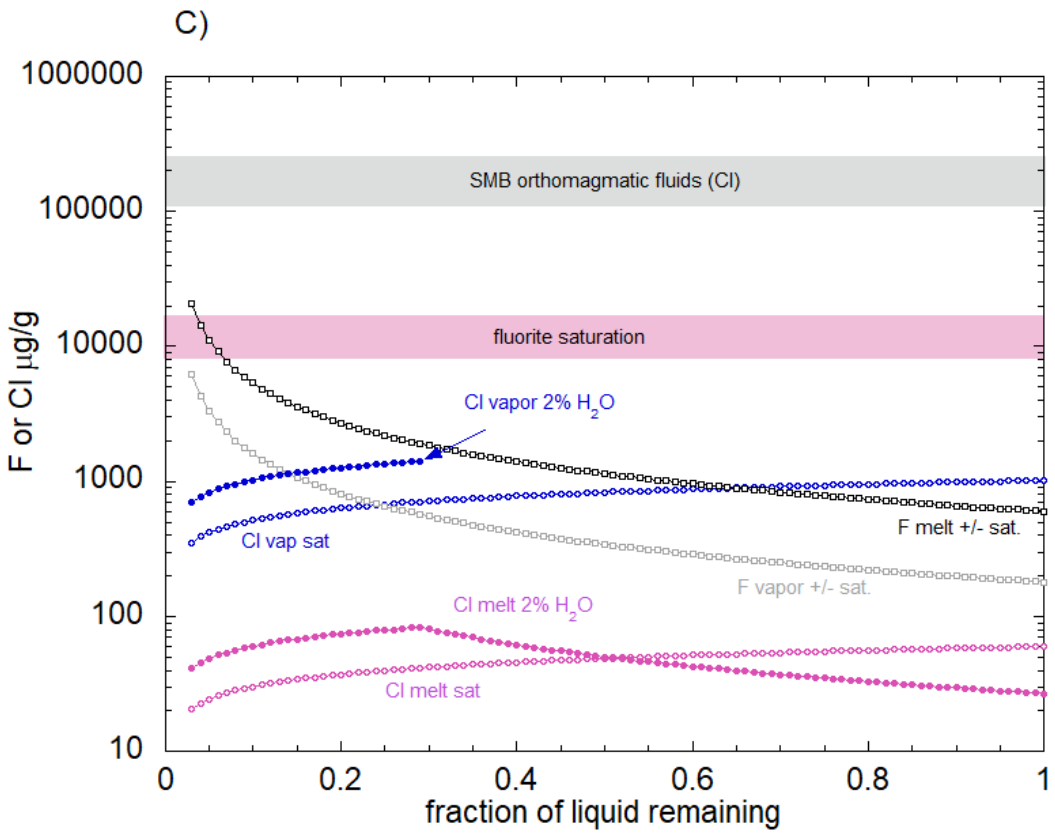

Figure 8 (and previous page). Comparison between measured and modeled biotite F, Cl and OH compositions from Stage 1 and Stage 2 plutons of the SMB. **A)** Mole fraction of endmember F, Cl and OH components in biotite as a function of the biotite Ti concentration. The model curves correspond to the calculated biotite compositions assuming fractional crystallization of an initial melt with 600 µg/g F, 27 (2% water) or 60 (water saturated) µg/g Cl and 0.11 wt% Ti using biotite-melt exchange and partition coefficients for F-OH, Cl-OH and Ti extracted from the experimental data of Icenhower and London (1995; 1997). The model curve with x ticks is calculated for MVP saturation throughout crystallization, whereas the model curve with vertical ticks assumes the melt is initially water undersaturated with 2 wt%, but reaches MVP saturation during crystallization (f = 0.29; demarcated by the inflection point in the model curves). The model curves range from a liquid fraction, F = 1 (~2.5 wt% Ti in biotite) to F= 0.03 (~0.7 wt% Ti in biotite) in increments of 0.01. **B)** Ternary OH/10-Clx10-F diagram portraying the mole fraction endmember compositions and the same model curves as per A). In each case, the starting point at 100% liquid (F=1) is indicated. Values of F along model curves are liquid fraction remaining. See text for further details, and Table 2 for a summary of model parameters. **C)** Calculated concentrations of Cl and F in melt and MVP as a function of the fraction of liquid remaining for the crystallization models presented in A) and B). The gray field corresponds to the range of Cl concentrations in fluid inclusions from the East Kemptville Sn deposit (27-41 wt% NaCl equivalent) associated with the Davis Lake Pluton reported by Halter et al. (1995) and from the Sn-W-Cu-U-Mn deposits (19-25 wt% NaCl equivalent) associated with the New Ross and Salmon Tail Lake plutons (Carruzzo et al., 2004). The field labeled fluorite saturation corresponds to the fluorine content of the melt at fluorite saturation (8000-18,000 µg/g) measured by Icenhower and London (1997).